Mon. Not. R. Astron. Soc. **000**, 1–26 (2014) Printed 2 February 2022 (MN LaTeX style file v2.2)

The MassiveBlack-II Simulation: The Evolution of Halos and Galaxies to $z \sim 0$

Nishikanta Khandai[1], Tiziana Di Matteo[2], Rupert Croft[2], Stephen Wilkins[3], Yu Feng[2], Evan Tucker[2], Colin DeGraf[4], Mao-Sheng Liu[2]

[1] *Brookhaven National Laboratory, Department of Physics, Bldg 510, Upton, NY 11973, USA*
[2] *McWilliams Center for Cosmology, Carnegie Mellon University, 5000 Forbes Avenue, Pittsburgh, PA 15213, USA*
[3] *Astronomy Centre, Department of Physics and Astronomy, University of Sussex, Brighton, BN1 9QH, U.K.*
[4] *Racah Institute of Physics, The Hebrew University, Jerusalem 91904, Israel*

2 February 2022

ABSTRACT

We investigate the properties and clustering of halos, galaxies and blackholes to $z = 0$ in the high resolution hydrodynamical simulation MassiveBlack-II (MBII). MBII evolves a ΛCDM cosmology in a cubical comoving volume of $V_{box} = (100\mathrm{Mpc/h})^3$ and is able to resolve halos of mass $M_{\rm halo} = 10^9 M_\odot$/h. It is the highest resolution simulation of this size which includes a self-consistent model for star formation, black hole accretion and associated feedback. We provide a simulation browser web application which enables interactive search and tagging of halos, subhalos and their properties and publicly release our galaxy catalogs to the scientific community. Our analysis of the halo mass function in MBII reveals that baryons have strong effects, with changes in the halo abundance of 20-35% below the knee of the mass function ($M_{\rm halo} \lesssim 10^{13.2} M_\odot$/h at $z = 0$) when compared to fits based on dark matter only simulations. We provide a fitting function for the halo mass function valid for the full range of halo masses in MBII out to redshift $z = 11$ and discuss how the onset of non-universal behavior in the mass function limits the accuracy of our fit. We examine the halo occupation distribution of satellite galaxies and present results valid over 5 orders of magnitude in host halo mass. We study the clustering of galaxies, and in particular the evolution and scale dependence of stochasticity and bias. Comparison with observational data for these quantities for samples with different stellar mass thresholds yields reasonable agreement. Using population synthesis, we find that the shape of the cosmic spectral energy distribution predicted by MBII is consistent with observations, but lower in amplitude. The Galaxy Stellar Mass Function (GSMF) function is broadly consistent with observations at $z \geq 2$. At $z < 2$, observations probe deeper into the faint end and the population of passive low mass (for $M_* < 10^9 M_\odot$) galaxies in the simulation makes the GSMF too steep. At the high mass end ($M_* > 10^{11} M_\odot$) galaxies hosting bright AGN make significant contributions to the GSMF. The quasar bolometric luminosity function is also largely consistent with observations. We note however that more efficient AGN feedback (beyond simple thermal coupling used here) is likely necessary for the largest, rarest objects/clusters at low redshifts.

Key words: methods: numerical – cosmology: theory – cosmology: large-scale structure of Universe – galaxies: formation – galaxies: evolution – quasars: general

1 INTRODUCTION

The Cold Dark Matter model with a cosmological constant (ΛCDM) is well established enough (see e.g., Planck Collaboration et al. 2013,Hinshaw et al. 2013, Lahav & Liddle 2014,Crandall & Ratra 2013) that individual large-scale simulation efforts can be carried out that focus on just this one cosmology. We have also reached the point at which supercomputers enable numerical modeling of cosmological volumes with enough resolution to study the properties of individual galaxies. In this paper we report on a P-GADGET hydrodynamic simulation of $100h^{-1}$Mpc cubic volume, the MassiveBlackII simulation. It has $\sim 10^6 M_\odot$ mass resolution, cooling, star formation, black holes and feedback, and represents the evolution of a ΛCDM universe to redshift $z = 0$.

Numerical simulations (see reviews by Dolag et al. 2008, Springel 2012, Bertschinger 1998) are the tool of choice to address many questions in cosmology, as galaxy formation is a complex non-linear problem. Two criteria which must be satisfied for accurate results are:

(1) A large enough simulation volume that Fourier density modes on the largest scales are evolving independently. The volume simulated must be a representative region of the Universe, otherwise inferences drawn from it regarding such questions as clustering and the mass function of objects will be incorrect (Bagla & Ray 2005, Bagla & Prasad 2006, Orban 2013). When ΛCDM models are evolved to redshift $z = 0$, then a volume of at least $\sim 100h^{-1}$Mpc on a side becomes necessary to predict the overall star formation rate, for example (Springel & Hernquist 2003).

(2) High enough mass and spatial resolution that the properties of the objects of interest have converged. This requires many resolution elements (particles or grid cells). If we focus on particle based simulations relevant to the current work, at the very least for identification of objects there must enough particles to overcome shot noise. If we require detailed properties of the objects such as galaxy spectra, or angular momenta then this can require many more (e.g., Governato et al. 2007).

These criteria of large simulation volume and high resolution are more straightforward to address in the context of more restricted physical modeling. As a result, dark matter and gravity-only simulations have long been used to make cosmological predictions that cover both large and small scales in the same volume (e.g., Springel et al. 2005, Boylan-Kolchin et al. 2009, Klypin, Trujillo-Gomez, & Primack 2011). Semi-analytic modeling has been used to process dark matter simulations, resulting in many studies of the galaxies and their properties in the ΛCDM model (see e.g., Baugh 2006, Hirschmann et al. 2012 and references therein).

Baryonic physics including hydrodynamics obviously plays an important role in the formation of luminous objects and structure. This has lead to the inclusion of the relevant equations in simulation codes in many forms, Smoothed Particle Hydrodynamics (SPH, Monaghan 1992), Eulerian grid solvers (e.g., Cen 1992, Bryan & Norman 1997) and hybrid Lagrangian/Eulerian schemes (e.g., Springel 2010). Although previous work has not simultaneously reached the combination of large volume and high resolution that we present here, research has progressed using many methods, including making use of zoom simulations of smaller volumes inside a representative one (Katz & White 1993, Scannapieco et al. 2012), simulations that stop at high redshifts before large-scale modes become non-linear (e.g., Di Matteo et al. 2012), or by tackling problems which require lower mass resolution (e.g., Battaglia et al. 2012).

The advent of large-scale computing facilities with 100,000 compute cores or more (such as the Cray XT5, "Kraken" on which the current simulation was run) and the development of highly efficient distributed memory simulation codes (such as GADGET2, Springel 2005) means that simulations which satisfy both criteria (1) and (2) are now possible. We have run one such simulation as part of the NSF Petascale Applications in Cosmology program, using the code P-GADGET (see e.g., Di Matteo et al. 2012).

Our aim was to simulate and analyze a large, representative volume of the ΛCDM model with the most important physical processes previously included in zoom runs or simulations with smaller boxes. These are hydrodynamics (using SPH), cooling, a subgrid multiphase model for star formation (Springel & Hernquist 2003) and subgrid black hole modeling (Springel, Di Matteo, & Hernquist 2005,Di Matteo, Springel, & Hernquist 2005), both with feedback. Our use of the physical modeling and algorithms used in previous work such as Di Matteo et al. (2008), Croft et al. (2009), Degraf, Di Matteo, & Springel (2010) and Di Matteo et al. (2012) enables continuity and therefore comparison with this previous work. Our aim is to see what this "fiducial" model (ΛCDM + GADGET SPH + the particular subgrid algorithms employed) predicts about the properties of galaxies, their halos and their clustering at redshifts extending down to the present day. We have not adjusted methods, algorithms and parameters used in previous work (e.g., DeGraf et al. 2012) to try to tune to observational results. Our goal is to see how this model performs, now that there is a large volume at high resolution. We naturally expect both regions of agreement and disagreement with observations and we aim that our work will offer guidance to future work to address the problems.

In this paper, we make the first use of the MassiveBlackII simulation evolved to $z = 0$, and use it to explore some topics in structure formation. Here we choose to focus on topics relevant to galaxy and AGN formation and large-scale structure, including mass functions, galaxy and halo properties and clustering. Our emphasis is on lower redshifts; the simulation at redshifts $z > 5$ has been explored by Wilkins et al. (2013), Wilkins et al. (2013), and Wilkins et al. (2013). Topics that we leave to future work include the intergalactic medium, absorption lines, galaxy clusters and X-ray emission.

Our plan for the paper is as follows. In Section 2 we briefly describe the numerical methods and algorithms used to run the simulation, select galaxies and carry out stellar population synthesis. In Section 3, we describe visualization of the simulation. In Sections 4 and 5 respectively we present the mass function and halo occupation distribution and in Section 6 we examine the clustering of dark matter and galaxies. The properties of galaxies and supermassive black holes are examined in Sections 7 and 8 and we derive some conclusions from our work in Section 9.

2 METHODS:

2.1 Numerical Code

We have used P-GADGET, an upgraded version of GADGET3 (see Springel (2005) for an earlier version) which we are developing for use at upcoming Petascale supercomputer facilities. This code was also used to run the MassiveBlack (MB) simulation (Di Matteo et al. (2012). Both MB and MBII are cosmological simulation of a ΛCDM cosmology. The major differences between MB and MBII are resolution and volume. However there are minor differences in cosmology between the two.

The initial conditions for MBII were generated with the CMBFAST transfer function at $z = 159$ and the simulation was evolved to $z = 0$. The cosmological parameters used

$L_{\rm box}$ $(h^{-1}{\rm Mpc})$	$N_{\rm part}$	$m_{\rm DM}$ $(h^{-1}M_\odot)$	$m_{\rm gas}$ $(h^{-1}M_\odot)$	ϵ $(h^{-1}{\rm kpc})$
100	2×1792^3	1.1×10^7	2.2×10^6	1.85

Table 1. Basic simulation parameters for the simulation. The columns list the size of the simulation box, $L_{\rm box}$, the number of particles (dark matter + gas) used in the simulation, $N_{\rm part}$, the mass of a single dark matter particle, $m_{\rm DM}$, the initial mass of a gas particle, $m_{\rm gas}$, and the gravitational softening length, ϵ. All length scales are in comoving units.

were: amplitude of mass fluctuations, $\sigma_8 = 0.816$, spectral index, $n_s = 0.968$, cosmological constant parameter $\Omega_\Lambda = 0.725$, mass density parameter $\Omega_m = 0.275$, baryon density parameter $\Omega_b = 0.046$ and $h = 0.701$ (Hubble's constant in units of $100{\rm km\,s^{-1}Mpc^{-1}}$). These are consistent with the WMAP7 cosmology (Komatsu et al. 2011).

2.2 Halo And Subhalo Identification

We identify halos with the friends-of-friends (FOF) procedure (Davis et al. 1985) applied to dark matter particles with a linking length of $b = 0.2$ times the mean inter-particle separation. Gas, stars and BHs are then associated to their nearest dark matter particles. The subhalo finder SUBFIND (Springel et al. 2001) was then used, working with particles in the FOF halo and computing a local density for each particle. Starting from isolated density peaks within the FOF halo, additional particles with decreasing density are attached to it. Whenever a saddle point, which connects two disjoint overdensities is reached, the smaller of the two is treated as a substructure candidate followed by merging of the two regions. Eventually all particles within a substructure are checked for self-boundedness and only those particles are retained which have a total negative energy.

2.3 Subgrid Model for Star Formation BH growth and associated feedback

The subgrid models for star formation, BH growth and associated feedback processes are identical to that employed in the MB simulation. We briefly describe them here and refer the reader to the MB simulation (e.g., Di Matteo et al. (2012)) for a more detailed description.

We adopt the multiphase model for star forming gas developed by Springel & Hernquist (2003). This has two principal ingredients: (1) a star formation prescription and (2) an effective equation of state (EOS). (1) is motivated by observations and given by the Schmidt-Kennicutt Law (Kennicutt 1989), where the star formation rate is proportional to the density of cold clouds ($\rho_{\rm SFR} \propto \rho_{gas}^N$ and $N = 1.5$. Star particles are created from gas particles probabilistically according to their star formation rates. (2) encapsulates the self-regulated nature of star formation due to supernovae feedback in a simple model for a multiphase ISM. In this model, a thermal instability is assumed to operate above a critical density threshold $\rho_{\rm th}$, producing a two phase medium consisting of cold clouds embedded in a tenuous gas at pressure equilibrium. Stars form from the cold clouds, and short-lived stars supply an energy of 10^{51} ergs to the surrounding gas as supernovae. This energy heats the diffuse phase of the ISM and evaporates cold clouds, thereby establishing a self-regulation cycle for star formation. $\rho_{\rm th}$ is determined self-consistently in the model by requiring that the EOS is continuous at the onset of star formation. The cloud evaporation process and the cooling function of the gas then determine the temperatures and the mass fractions of the two 'hot and cold' phases of the ISM, such that the EOS of the model can be directly computed as a function of density. In addition, a parametrization of stellar winds is also used (see Springel & Hernquist 2003, for further details).

In MBII BHs are modeled as collisionless sink particles within newly collapsing halos, which are identified by the FOF halofinder called on the fly at regular time intervals. A seed BH of mass $M_{\rm seed} = 5\times10^5 h^{-1}M_\odot$ is inserted into a halo with mass $M_{\rm halo} \geq 5\times10^{10}h^{-1}M_\odot$ if it does not already contain a BH. Once seeded, BHs grow by accreting gas in its surrounding region or by merging with other BHs. Gas is accreted with an accretion rate $\dot{M}_{\rm BH} = \frac{4\pi G^2 M_{\rm BH}^2 \rho}{\left(c_s^2+v_{\rm BH}^2\right)^{3/2}}$, where $v_{\rm BH}$ is the velocity of the black hole relative to the surrounding gas, ρ and c_s are the density and sound speed of the hot and cold phase of the ISM gas (which when taken into account appropriately as in Pelupessy, Di Matteo, & Ciardi (2007) eliminates the need for a correction factor α previously introduced). We allow the accretion rate to be mildly super-Eddington but limit it to a maximum allowed value equal to 2×Eddington rate ($\dot{M}_{\rm Edd}$) to prevent artificially high values, consistent with Begelman, Volonteri, & Rees (2006); Volonteri & Rees (2006). The BH radiates with a bolometric luminosity which is proportional to the accretion rate, $L_{\rm bol} = \eta\dot{M}_{\rm BH}c^2$ (Shakura & Sunyaev 1973), where η is the radiative efficiency and its standard value of 0.1 is kept throughout, and c is the speed of light. In the simulation 5% of the radiated energy couples thermally to the surrounding gas and this energy is deposited isotropically on gas particles that are within the BH kernel (64 nearest neighbors) and acts as a form of feedback (Di Matteo, Springel, & Hernquist 2005). The value of 5% is the only free parameter in the model and was set using galaxy merger simulations (Di Matteo, Springel, & Hernquist 2005) to match the normalization in the observed $M_{\rm BH} - \sigma$ relation. BHs also grow by merging once one BH comes within the kernel of another with a relative velocity below the local gas sound speed.

This model for the growth of BHs has been developed by Di Matteo, Springel, & Hernquist (2005); Springel, Di Matteo, & Hernquist (2005). It has been implemented and studied extensively in cosmological simulations (Sijacki et al. 2007; Li et al. 2007; Colberg & Di Matteo 2008; Di Matteo et al. 2008; Croft et al. 2009; Booth & Schaye 2009; Sijacki, Springel, & Haehnelt 2009; Degraf, Di Matteo, & Springel 2010; Degraf et al. 2011c,b; Chatterjee et al. 2012), successfully reproducing basic properties of BH growth, the observed $M_{\rm BH} - \sigma$ relation and the BH mass function (Di Matteo et al. 2008), the quasar luminosity function (Degraf, Di Matteo, & Springel 2010) and the clustering of quasars (Degraf et al. 2011c).

2.4 Stellar Population Synthesis

The spectral energy distribution (SED) of a galaxy is generated by summing the SEDs of each star particle in the

galaxy. The SED of the star particles is generated using the Pegase.2 stellar population synthesis (SPS) code (Fioc & Rocca-Volmerange 1997, 1999) by considering their ages, mass and metallicities and assuming a Salpeter IMF. Nebula (continuum and line) emission is also added to each star particle SED. We also apply a correction for absorption in the intergalactic medium (IGM) using the standard Madau et al. (1996) prescription. We finally sum the SED of each galaxy and convolve with given filters (see bottom panels of figure 17) to finally obtain the broadband photometry, hence the CSED.

2.5 Public Release of MBII Galaxy Catalogs

We release the MBII galaxy catalogs to the scientific community. Some of the properties included in these catalogs are position, velocity, mass, mass by particle type (such as gas, dark matter, stars and BHs), circular velocity and rest-frame luminosities. We encourage the community to use these galaxy catalogs which can be accessed from *http://mbii.phys.cmu.edu/data/*. A more detailed description and sample codes can also be found at the above URL.

3 VISUALIZATION

To enable easy visual exploration of the large dataset represented by the MassiveBlack 2 simulation, we have developed an interactive simulation browser web-application. The browser allows real-time zooming, panning in the simulation, and enables searching and locating of halos and subhalos in the simulation. The application is built upon existing web technology. Two main libraries used are Gigapan[1], and the Microsoft Seadragon library [2].

Figure 1 shows the interface for the interactive browser. The browser can be accessed from the URL *http://mbii.phys.cmu.edu* . It consists of a viewport and three floating control panels: the MAIN panel, located at the top-right corner of the interface; the INFOrmation panel, located at the left side of the interface; and the NAVigation panel, located at the bottom right corner of the interface.

The Gigapan image of the selected snapshot is displayed in the viewport, where subhalos are also marked with green crosses. In addition, central subhalos ($M_{\rm subhalo} > 0.1 M_{\rm group}$) are labeled with an additional circle. Interactive zooming and panning in the viewport is implemented via mouse clicking and dragging.

The MAIN panel provides the following functionalities:

(i) selecting an epoch from the snapshot number;
(ii) switching between the gas and stellar image layer;
(iii) jumping among FOF groups;
(iv) querying subhalos in the current view.

The INFO panel displays the properties of the currently selected subhalo or group. In Figure 1, for example, the panels shows the property of the currently selected subhalo (marked with a rectangle).

[1] http://www.gigapan.org
[2] http://gallery.expression.microsoft.com/SeadragonAjax

The NAV panel provides zoom-in and zoom-out controls, and a switch to toggle the visibility of other control panels.

Figure 2 shows a collage of images extracted from the browser. In this example we have selected three halos in the simulation at redshift $z = 1.0$: (I) at a major confluence of filaments; (II) a moderately sized halo with three main subhalos; (III) a relatively isolated halo. For each of the halo we show the stellar component in their subhalos, embedded in their surrounding gas environment.

The gigapan images used in the browser are high resolution 2-D images of the full simulation rendered with the visualization software Gaepsi (Feng et al. 2011). The gas images (panels O, I, II, III) are rendered with the divergent Cool-Warm color-map introduced by Moreland (2009). The density information is encoded in the brightness of the pixels: brighter pixels have higher column density, and voids are represented with black (zero-brightness). The temperature of gas is encoded in the hue of the pixels, blue represents low temperature ($T < 10^{3.5}$ K), and red represents high temperature ($T > 10^{7.5}$ K). The stellar images (panels a, b, c, d, e, and f) are composed from the simulated i, r, and g band luminosity. This band definition follows the convention used by the Sloan Digital Sky Survey (see the procedure described in Lupton et al. 2004).

4 MASS FUNCTION OF HALOS

Given that dark matter halos represent the locations where gas can cool and form stars and galaxies it is important to predict their abundances - the halo mass function - accurately. The halo or subhalo mass function, is one of the fundamental quantities in structure formation. It is an important ingredient in a diverse set of tools used for making theoretical predictions in cosmology. At low redshifts the tail of the mass function which probes the abundance of clusters is extremely sensitive to cosmological parameters. It is also a key component in studying the clustering of galaxies as the halo-halo term (see Cooray & Sheth 2002) depends on the mass function. At higher redshifts the mass function is used in modeling the sources of reionization which reside in dark matter halos like PopIII stars, early galaxies and quasars. Any significant deviation in the mass function as predicted by the ΛCDM model would therefore create some tension in our current understanding of structure formation.

Traditionally dark matter simulations have been used to compute the abundance of halos for a given cosmology. A key component of these analyses is the halo definition. The FOF definition identifies regions bounded by an isodensity contour whereas the Spherical Overdensity (SO) definition identifies an artificial spherical region centered on a density maximum such that the density within it is at a given density threshold. A dark matter halo is never perfectly spherical making the SO definition artificial. The FOF definition is prone to artificially bridging two (or more) nearby halos connected by a filament.

In this section we will not look at how the halo definition affects the mass function predicted by MBII since much work has been done on this subject (Lacey & Cole 1994; Jenkins et al. 2001; White 2002; Tinker et al. 2008; Watson et al. 2013). We will rather choose a halo definition and see how baryonic

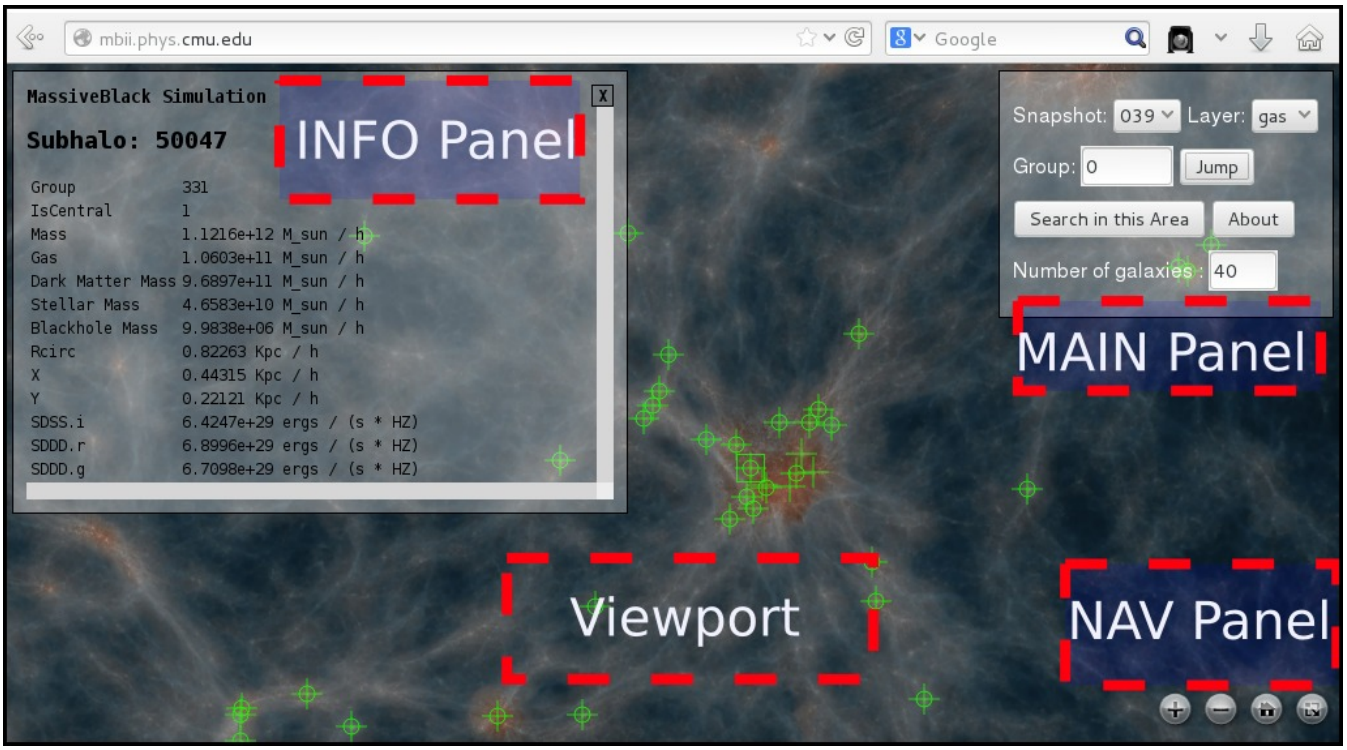

Figure 1. Interface for the interactive simulation browser.

effects affect the mass function and compare our results with fitting functions based on dark matter only simulations.

We generate two catalogues of halos based on the FOF and SUBFIND halofinders. These catalogues contain the total number of particles by type (e.g. gas, dark matter, stars and BHs), and the total mass by type amongst other important halo properties. For the analysis in this section we consider the smallest halo to have a resolution limit of 40 particles by type. E.g. An object is considered to be a halo if its mass satisfies $M_{\rm halo} \geq 40 \times (m_{dm} + m_{gas})$, where m_{dm} and m_{gas} are given in table 1. If we are interested only in the dark matter component of the halo then the above condition is relaxed such that $M_{\rm halo} \geq 40 \times m_{dm}$. Note that these criteria affect the statistics and counts of only the smallest halos.

In the case of dark matter simulations it has been shown (Warren et al. 2006) that halos with small particle counts have a mass which is systematically overestimated. Corrections have been proposed to alleviate this (Warren et al. 2006; Lukić et al. 2009; Bhattacharya et al. 2011; More et al. 2011). We choose to ignore for this effect for two reasons. (1) It is not clear how such corrections apply to each particle type in MBII. Providing a similar correction to halo masses for hydrodynamical simulations is beyond the scope of this paper. (2) In section 4.2 we will show that the baryonic effects already show up in the halo mass function at lower masses at the 10-35% level when compared to dark matter simulations. A correction to the mass of the halo at smaller masses will only enhance the discrepancy in the mass function.

The largest mode that any cosmological simulation can sample is governed by the physical size of the simulation volume. Large scale modes $k < 2\pi/L_{box}$ are not sampled in the simulation and lead to a suppression of structure formation and hence the mass function. This is a well known effect (Bagla & Ray 2005; Sirko 2005; Bagla & Prasad 2006) and masses can be corrected by accounting for the missing power (Reed et al. 2007; Watson et al. 2013). Bagla & Ray (2005) point out that a boxsize $L_{box} = 100h^{-1}$Mpc is sufficient to obtain reasonably reliable mass functions to halo masses $M_{\rm halo} \lesssim 10^{14} M_\odot$/h for the ΛCDM model at $z = 0$; the requirement for large boxes becomes less stringent at higher redshift. Our focus will in any case be for smaller masses, which are less affected by effects of finite volume. We therefore choose not to make any corrections to the mass function due to missing large scale power.

4.1 The baryon fraction of halos

We start by looking at the baryon fraction of halos in figure 3 as a function of halo mass. We plot the ratio of the baryon fraction of halos to the cosmic baryon fraction f_b^{halo}/f_b^{cosmic} where $f_b^{cosmic} = \Omega_b/\Omega_m$ and f_b^{halo} is the ratio of baryonic to total mass of the halo. The solid line represents halos identified with the FOF algorithm whereas the dot-dashed line represents those identified by SUBFIND.

We find that the distinction between halos and subhalos has little effect on the baryon fraction of halos below $z = 6$. At $z \geq 6$ the baryon fraction of subhalos identified with SUBFIND is larger compared to objects identified with FOF although the qualitative trend with mass is similar. We find that the baryon fraction plateaus to around 80-90% around $M_{\rm halo} \geq 10^{13} M_\odot/h$ at low redshifts and drops significantly below that mass scale. At this point it is worthwhile to compare our results with Crain et al. (2007) who looked at the baryon fraction of halos in an adiabatic resimulation of the

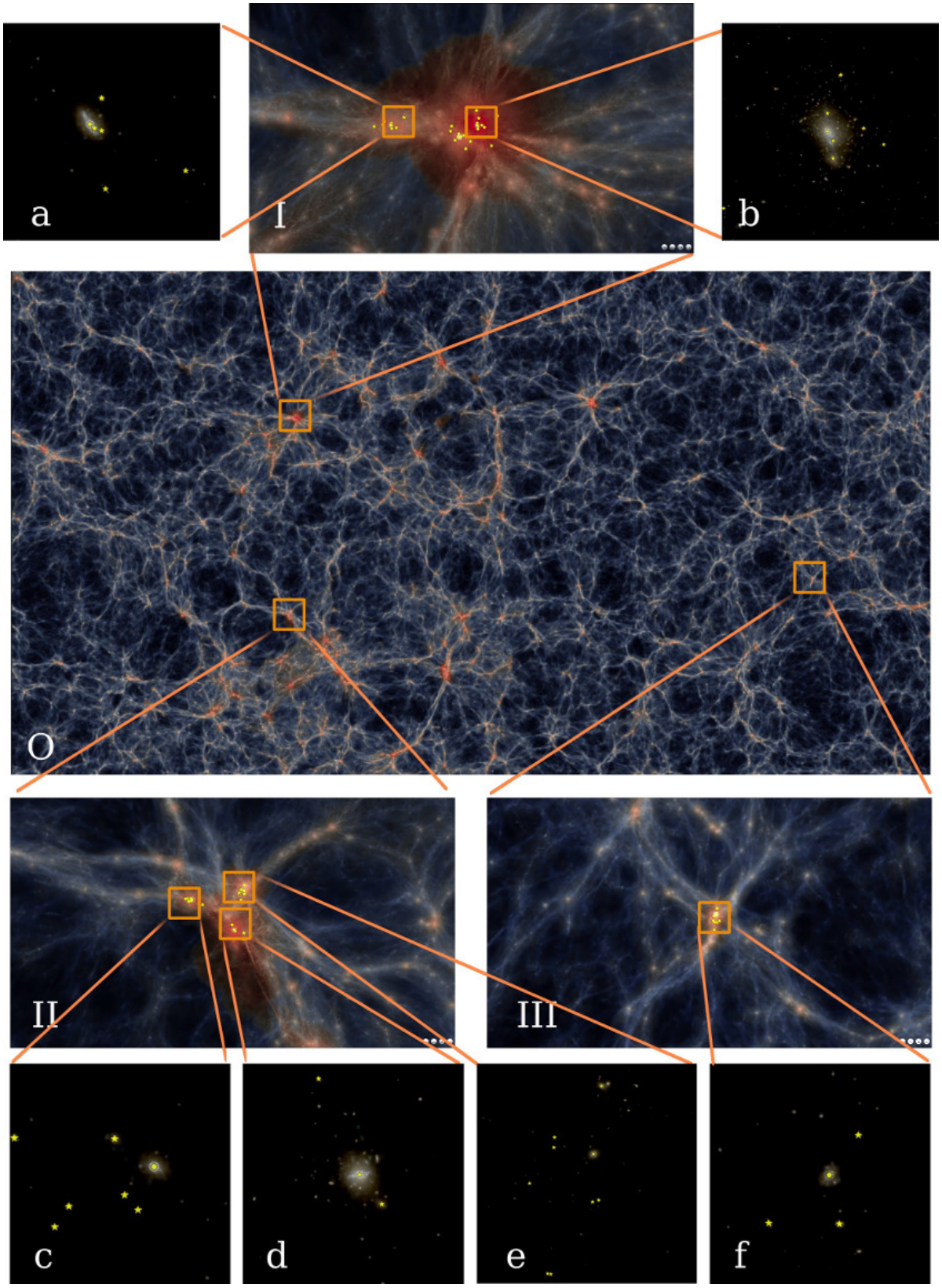

Figure 2. Visualization of MBII simulation. The central panel, O shows the full simulation box: the $z = 1.0$ snapshot is mapped into a $8\,h^{-1}$Mpc thick slice. Panels I, II, and III show the gaseous environment of three FOF groups. Panel a to f show the stellar component of the subhalos. The central subhalos are marked with dots, and 10 of the brightest subhalos are marked with stars. Please see text for a description of the color scheme. The interactive simulation browser is available at http://mbii.phys.cmu.edu .

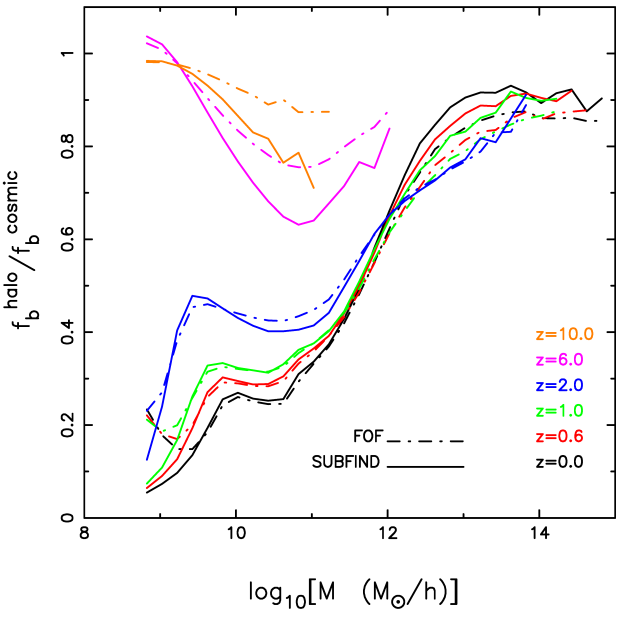

Figure 3. The evolution of the baryon fraction of halos (f_b^{halo}) in units of the cosmic baryon fraction f_b^{cosmic} as a function of halo mass. The solid line is for FOF halos and the dot-dashed is for halos identified with SUBFIND. The colors (black, red, green, blue, pink and orange) represent the baryon fraction for different redshifts ($z = 0.0, 0.6, 1, 2, 6, 10$)

Millennium simulation and another smaller volume (higher resolution) simulation at $z = 0$. These authors also included an additional simulation with a simple photoheating model, where a gas temperature floor of $T_{floor} = 2 \times 10^4$K was assumed to mimic the IGM temperature at mean density in the post-reionized Universe. Star and blackhole formation and associated feedback processes were not included. These authors found that the baryon fraction plateaued to around 90% for $M_{\rm halo} \geq 10^{10} M_\odot/h$ and dropped significantly below that in their photoionisation model, whereas the baryon fraction in the adiabatic simulation did not show any significant behavior with halo mass. Our results largely agree well the results of Crain et al. (2007), for larger masses however, we find that feedback can drastically prevent the collapse of baryons in halos below $M_{\rm halo} \lesssim 10^{13} M_\odot/h$. Crain et al. (2007) found that photoionisation regulates the formation of smaller galaxies with $M_{\rm halo} \lesssim 10^{10} M_\odot/h$. Interestingly we find that at $M_{\rm halo} \sim 10^{10} M_\odot/h$ the baryon fraction plateaus to around 20-40% of the cosmic mean. It drops below that mass scale, which can be attributed to photoheating. The suppression of the baryonic fraction in $M_{\rm halo} = 10^{10} - 10^{13} M_\odot/h$ can be attributed to feedback from stars and blackholes.

Since we see that baryon effects play an important role in the formation of halos we expect to see deviations in the halo mass function which is the premise of the next section.

4.2 The mass function

We use the FOF and SUBFIND algorithms to compute the halo and subhalo mass functions respectively. We look at the total halo/subhalo mass and the mass of the dark matter component. In section 7 we will look at the galaxy stellar mass function (GSMF) and compare them with observational constraints. In this analysis we choose the mass bin to be $\Delta \log M = 0.2$ which is well within the recommended bin width (Lukić et al. 2007) to avoid any systematic error that may arise in the estimate of the mass function due to large bins. We assume Poisson errors for the counts of halos in this mass bin.

It is convenient to rewrite the differential mass function, $dn/d\log_{10} M$, in a rescaled form, $f(\sigma)$, which is independent of redshift, power spectrum and cosmology (Lacey & Cole 1994). The computed differential mass function $dn/d\log_{10} M$ can be rescaled to $f(\sigma)$

$$\frac{dn}{d\log_{10} M} = \frac{M}{\rho} \frac{d\ln \sigma^{-1}}{d\log_{10} M} f(\sigma) \qquad (1)$$

where M is the halo mass, ρ is the mean matter density and the variance in mass, smoothed with a real-space spherical top hat filter $W(k, M)$ at a scale $R(M) = (3M/4\pi\rho)^{1/3}$, is instead used as a mass variable and is given by

$$\sigma^2(M, z) = \frac{D_+(z)^2}{2\pi^2} \int_0^\infty k^3 P(k) W^2(k, M) d\log k \qquad (2)$$

The redshift dependence is encapsulated in the growth factor $D_+(z)$ which is normalized to $D_+(0) = 1$. $W(k, M)$. When written in this form equation 1 is universal since the dependence of redshift, power spectrum and cosmology are absorbed into the variable $\sigma(M, z)$. Therefore $f(\sigma)$ at multiple redshifts should fall on a single curve. The commonly and most used mass functions, namely the Press-Schecter (Press & Schechter 1974) and Sheth-Tormen (Sheth & Tormen 1999) mass functions, can then be written in a compact form:

$$f_{\rm PS} = \sqrt{\frac{2}{\pi}} \frac{\delta_c}{\sigma} \exp\left[-\frac{\delta_c^2}{2\sigma^2}\right] \qquad (3)$$

$$f_{\rm ST} = A\sqrt{\frac{2a}{\pi}} \left[1 + \left(\frac{\sigma^2}{a\delta_c^2}\right)^p\right] \frac{\delta_c}{\sigma} \exp\left[-\frac{a\delta_c^2}{2\sigma^2}\right] \qquad (4)$$

where, $\delta_c = 1.686$ is the linearly extrapolated overdensity of a spherical top-hat density perturbation at virialization in an Einstein-de Sitter Universe. For the Sheth-Tormen(Sheth & Tormen 1999) mass function $(A, a, p) = (0.3222, 0.707, 0.3)$ are additional parameters which better describe the shape of the mass function when compared to simulations.

In figure 4 we plot the rescaled mass function $f(\sigma)$ for redshifts $z = 10$ to $z = 0$ from the MBII simulation (open squares, blue to red). For the FOF mass functions we also add data from the MB simulation from redshifts $z = 11$ to $z = 5$ (open circles purple to green). For any simulation the mass function data points move from right to left along a single curve in the $f(\sigma) - \sigma$ plane. The top row and bottom rows denote the SUBFIND and FOF mass functions. The columns denote the full mass of the halo and the dark matter mass of the halo respectively. The dashed (red), dot-dashed (cyan), dot-dot-dot-dashed (orange) lines are for the mass functions from Press & Schechter (1974); Sheth & Tormen (2002); Watson et al. (2013) The solid (black) line in the bottom panels (FOF mass functions) denote the best fit mass function to the MB and MBII data based on the Tinker et al. (2008) parametrization of the Warren et al. (2006) mass function.

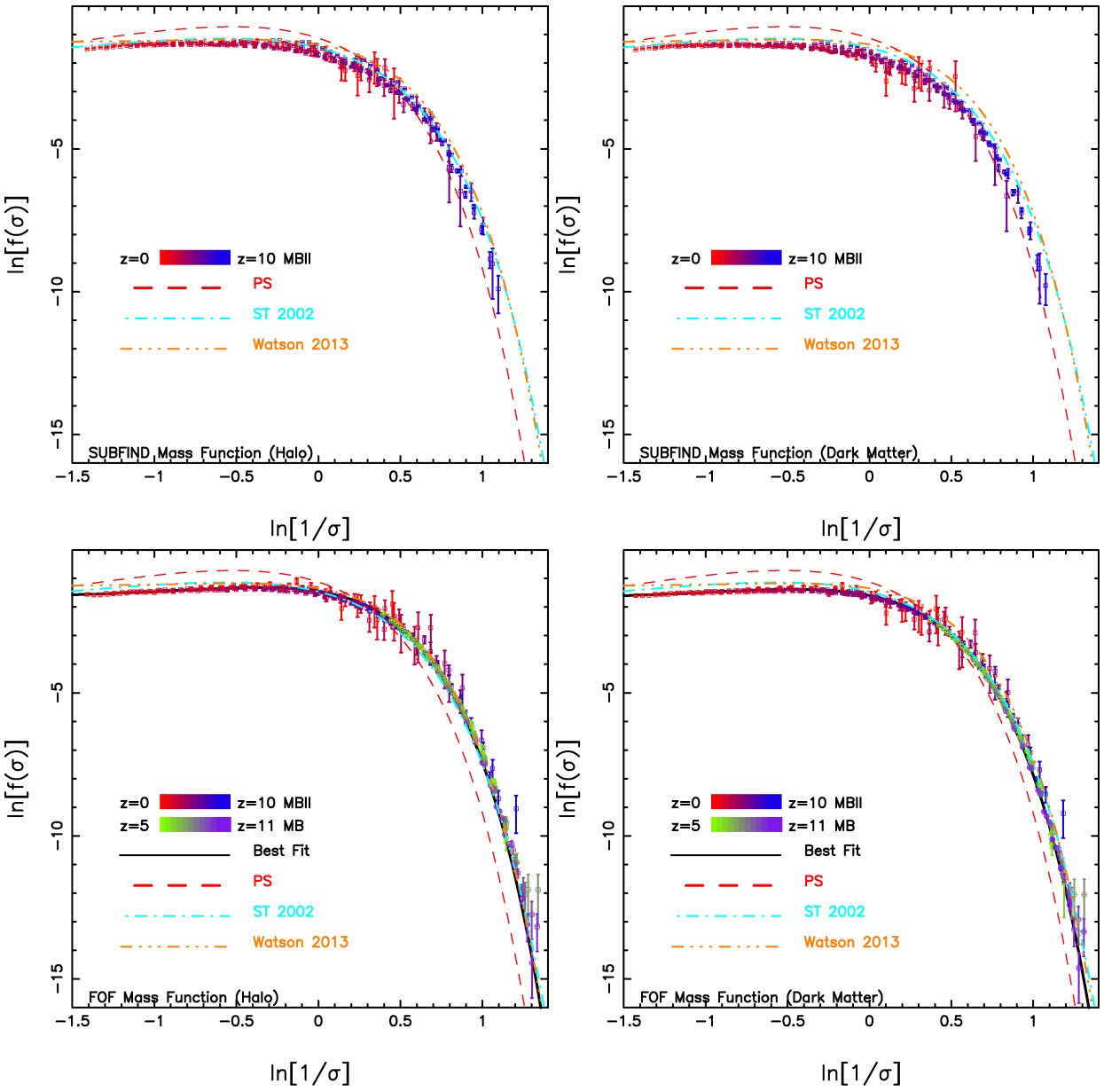

Figure 4. The SUBFIND (top) and FOF (bottom) mass functions are plotted from $z = 0 - 11$. The columns denote the mass function based on the total halo mass and the dark matter component of the halo mass respectively. The open squares denote data points from the MBII simulation from $z = 0 - 10$ (red-blue). The open circles in the FOF mass function (bottom panels) denote data from the MB simulation from $z = 5 - 11$ (green-purple). The dashed (red), dot-dashed (cyan), dot-dot-dot-dashed (orange) lines are for the mass functions from Press & Schechter (1974); Sheth & Tormen (2002); Watson et al. (2013). The solid (black) line in the bottom panels (FOF mass functions) denote the best fit mass function to the MB and MBII data based on the Tinker et al. (2008) parametrization of the Warren et al. (2006) mass function.

The PS mass function (Press & Schechter 1974) overpredicts the abundance of low mass halos and underpredicts the abundance of large mass halos. This has been seen in numerous studies (Sheth & Tormen 1999; Jenkins et al. 2001; Lukić et al. 2007; Reed et al. 2007; Watson et al. 2013). This has led to a renewed effort in recent years to recalibrate the mass function of halos based on simulations.

We find that the SUBFIND mass functions for halos and dark matter do not fall on a single curve. There is significant and systematic scatter across redshifts at small masses. This is similar to the analyses of Jenkins et al. (2001); Tinker et al. (2008); Watson et al. (2013) who found a for an object definition different from FOF halos a less universal mass function (having a redshift dependence). We therefore do not provide a universal fit to the SUBFIND mass functions which show a strong redshift dependence.

On the other hand the FOF mass function has been shown to be more universal (Jenkins et al. 2001; Bhattacharya et al. 2011; Watson et al. 2013) and this is also seen in the lower panels of figure 4. We denote FOF and FOFD to represent the FOF halo and dark matter component of the FOF halo. We find that the FOF and FOFD

mass functions agree well with the Sheth & Tormen (2002); Watson et al. (2013) mass functions at the larger masses. The FOFD shows a systematic shift with respect to the FOF mass function due to a systematic shift in the halo mass, since baryon contribution has been subtracted from the halo mass. However the mass function at small masses is systematically underestimated in MBII. This discrepancy is larger for FOFD which is again due to a systematic shift in the halo mass. Our results are consistent with Sawala et al. (2013) who used the set of simulations described in Crain et al. (2009) to look at the effect of baryons on the abundance of halos. Sawala et al. (2013) compared the GIMIC (which include gas, dark matter, star formation and feedback) and the DMO (dark matter only) simulations (Crain et al. 2009) which were performed by resimulating at higher resolution an $18h^{-1}$Mpc spherical region of the Millennium simulation (Springel et al. 2005). Both the GIMIC and DMO runs were done with the same initial conditions making it possible to look at the effect of baryons on halo properties directly. They found that both simulations agree well on large scales however objects below $\sim 10^{12}M_{\odot}$ have systematically lower masses in the GIMIC simulation when compared to the DMO counterpart. This result translated to an overestimate of the abundance of structures in the DMO simulation, by approximately $\sim 10\%$ at $10^{11.5}M_{\odot}$ and $\sim 30\%$ at $10^{10}M_{\odot}$. We do not have a DMO version of the MBII simulation to make a direct comparison. We therefore make a comparison of the mass function in MBII with published results based on dark matter only simulations.

Given the binned FOF and FOFD mass functions we perform separate fits with the Tinker et al. (2008) parametrization of the Warren et al. (2006) mass function:

$$f(\sigma) = A\left[\left(\frac{\beta}{\sigma}\right)^{\alpha} + 1\right]\exp\left[-\frac{\gamma}{\sigma^2}\right] \quad (5)$$

The solid black line in the lower panels (FOF and FOFD) of figure 4 represents our fits to the mass function. For the FOF mass function we have also added data from the $\sim \times 150$ larger volume MB simulation from $z = 5 - 11$ (open circles). This is done to obtain a larger range at the tail of the mass function. The fitted mass function function for FOF and FOFD are good to within $\sim 13\%$ across the full range of masses and redshifts. This means that the universality of the mass function holds for the FOF and FOFD mass functions at the $\sim 13\%$ level. The best fit parameters are quoted in table 2. We have also added the latest fit from dark matter simulations described in Watson et al. (2013). Watson et al. (2013) also find that their fit is accurate to $\sim 10\%$ across all redshifts and provide redshift dependent fits to obtain greater accuracy. The tail of the mass function which is governed by γ is consistent with Watson et al. (2013). We however find that the best fit mass function in MBII systematically underpredicts the abundance of halos in the tail of the mass function, which is dominated by high redshift data points (with large error bars). Such a behavior is also seen in Watson et al. (2013) and can only be improved by assuming a redshift dependent fit, which we leave to a forthcoming paper.

We end this section by comparing the best FOF mass function (MBII +MB) to earlier earlier work in figure 5. We plot the ratio of the FOF mass functions in Jenkins et al. (2001); Sheth & Tormen (2002); Warren et al. (2006); Bhattacharya et al. (2011); Watson et al. (2013) (solid (red), dashed (cyan), dot-dashed (blue), dotted (green) and dot-dot-dot-dashed (orange) lines) to our fit (table 2) and focus our attention at smaller masses, i.e. the gray shaded box bounded by $-1.4 \leq \ln(1/\sigma) \leq -0.2$ which highlights the region below the knee of the mass function, where dark matter simulations systematically overpredict the abundance of halos. We find that all the fits based on the dark matter simulations overpredict the mass function at the $20 - 35\%$ level at around $\ln(1/\sigma) \simeq -0.9$ when compared to our fit. $\ln(1/\sigma) = -0.9$ corresponds to $M_{\rm halo} = 10^{11.2}M_{\odot}/{\rm h}$ at $z = 0$ and $M_{\rm halo} = 10^{9.3}M_{\odot}/{\rm h}$ at $z = 1$. Even at the right edge of the shaded region, i.e. $\ln(1/\sigma) = -0.2$ which corresponds to $M_{\rm halo} = 10^{13.2}M_{\odot}/{\rm h}$ at $z = 0$, dark matter simulations overpredict the FOF mass function at the 10-20% level. To our knowledge the large effect baryonic processes have in shaping the mass function has been neglected up to this point.

	A	α	β	γ
FOF (MB+MBII)	0.1897	1.9607	1.7880	1.2067
FOFD (MB+MBII)	0.1738	1.6907	1.8812	1.2104
Watson et al. (2013)	0.282	2.163	1.406	1.210

Table 2. Best fit parameters for the FOF and FOFD mass functions. The parameters are described in equation 5. The last row is the best fit parameters from Watson et al. (2013).

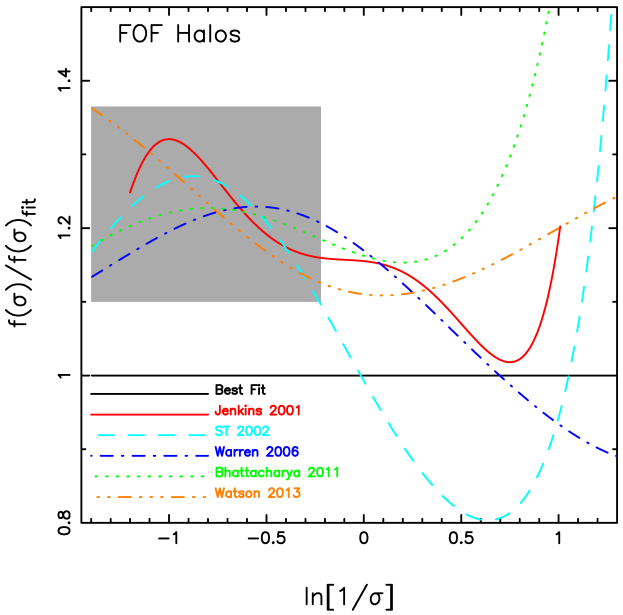

Figure 5. Ratio of the best fit FOF mass function with fits based on dark matter only simulations for FOF halos. The solid (black) horizontal line is for MBII. The solid (red), dashed (cyan) , dot-dashed (blue), dotted (green) and dot-dot-dot-dashed (orange) lines are from Jenkins et al. (2001); Sheth & Tormen (2002); Warren et al. (2006); Bhattacharya et al. (2011); Watson et al. (2013). The gray shaded box highlights the region below the knee of the mass function where dark matter simulations systematically overpredict the abundance of halos.

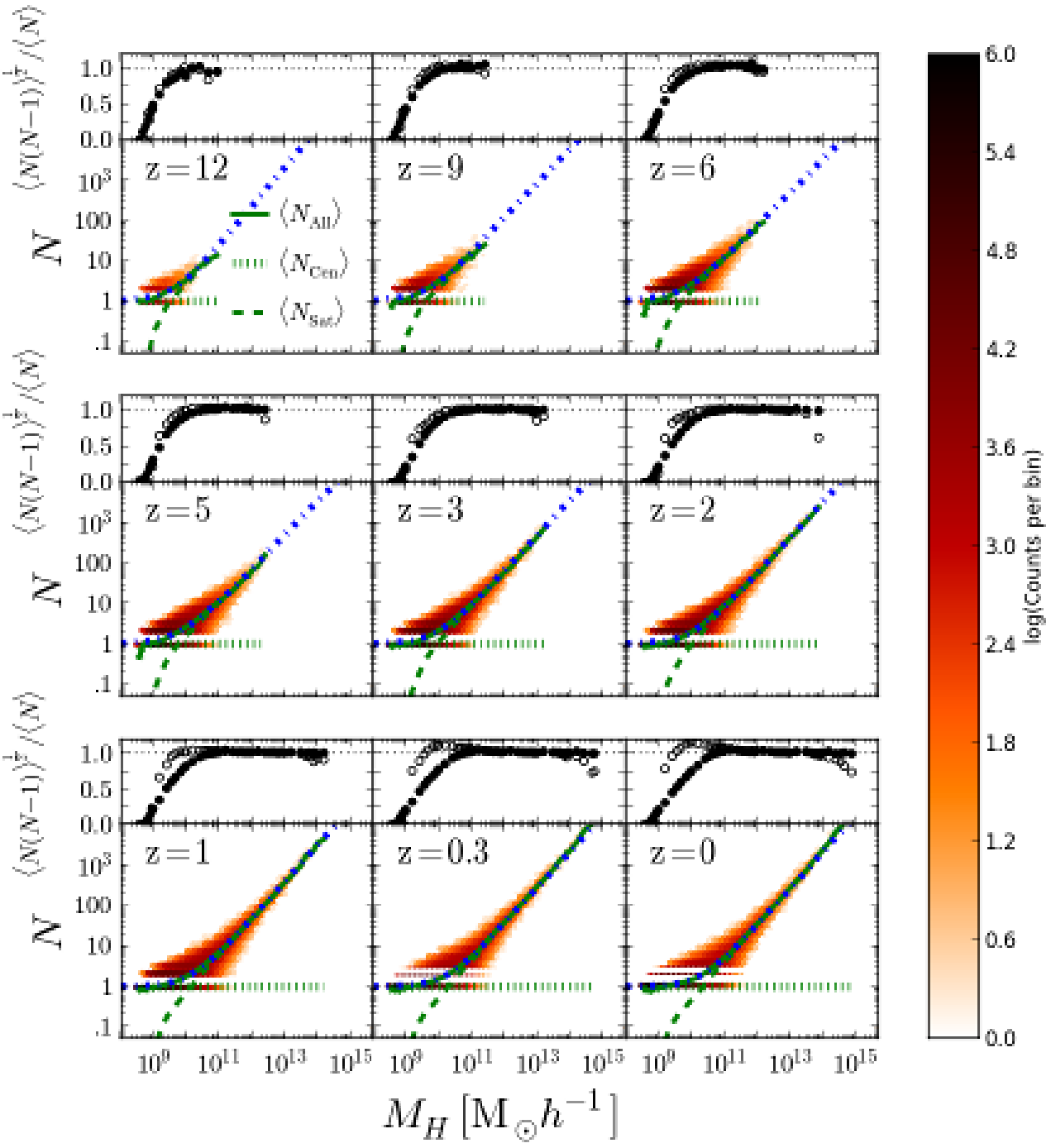

Figure 6. Occupation number and scatter of sub halos as a function of halo mass. The color corresponds to the log of the grid density at each occupation number and halo mass. The green over plotted curves are the mean occupation number of central sub halos(*dotted*), satellite sub halos (*dashed*), and all sub halos (*solid*). The blue dash-dotted curve is the best fit power law of the occupation number through all data points. The top panel for each is the width of the probability distribution for all sub halos (*solid circle*) and satellite sub halos (*open circle*). For a Poisson distribution, with width would be 1 which is the dotted line.

5 THE HALO OCCUPATION DISTRIBUTION

The Halo Occupation Distribution (HOD) is a powerful theoretical formalism used for describing, predicting, and interpreting the clustering of galaxies in the large scale structure of the universe. The HOD model describes the probability distribution $P(N|M_{\rm halo})$ that a halo with virial mass $M_{\rm halo}$ contains N galaxies. In addition to this probability distribution, the model also describes the relative spatial distribution of galaxies within the halo. Recently several papers have shown the robustness of the HOD by constructing and applying the model to large cosmological hydrodynamic simulations (e.g., White et al. (2001); Berlind & Weinberg (2002); Berlind et al. (2003); Zheng et al. (2005) and references therein). Like the recent hydrodynamic simulations, we will apply the HOD model to our own runs in this section. In the HOD model, the distribution of matter within a halo is described by two main components: first, the probability distribution $P(N|M_{\rm halo})$ that a halo with mass $M_{\rm halo}$ hosts N number of galaxies, and second, the relationship between the distribution of galaxies within the halos. In this section, we will briefly analyze and discuss these two components from our simulation.

The most important component of the HOD model is the probability distribution $P(N|M_{\rm halo})$. Figure 6 shows the occupation number N as a function of halo mass $M_{\rm halo}$ for nine snapshots. Each halo from the snapshots has one point on the plot and the color corresponds the log of the number of points per grid space. It is easy to see the power-law tail for high halo mass greater than $M_{\rm halo} \sim 10^{13}{\rm M}_{\odot}h^{-1}$ at almost all snap shots. However for high redshift, i.e. $z = 12$, there are few halos with $M_{\rm halo} > 10^{13}{\rm M}_{\odot}h^{-1}$, so the power-law tail isn't observed. The color plot corresponds to the total number of galaxies $N_{\rm All}$ as a function of halo mass, but the literature has shown that is is perhaps more robust to explore the occupation number of the central galaxy $N_{\rm Cen}$ and satellite galaxies $N_{\rm Sat}$ separately (Zheng et al. 2005). Previous studies have shown that a halo above a certain mass threshold will host one central galaxy, while halos below this mass threshold will not. Therefore, $N_{\rm Cen}$ can be modeled as a step function

$$N_{\rm Cen}(M_{\rm halo}) = \begin{cases} 0 & M_{\rm halo} < M_{\rm min} \\ 1 & M_{\rm halo} \geq M_{\rm min} \end{cases} \quad (6)$$

where $M_{\rm min}$ is the minimum mass of a halo which hosts a central galaxy. The green dotted lines in figure 6 is the average number of central galaxies $\langle N_{\rm Cen}\rangle$. For all snapshots $\langle N_{\rm Cen}\rangle$ plateaus at $N = 1$ quickly because nearly all halos identified with the FOF algorithm host one central galaxy. The halos that host a central galaxy can also be populated by satellite galaxies. The dashed green lines in figure 6 show the average number of satellite galaxies $\langle N_{\rm Sat}\rangle$. Like the occupation number of all galaxies, $\langle N_{\rm Sat}\rangle$ follows a power-law for halo masses greater than $M_{\rm halo} \sim M_1$, where M_1 is the mass of a halo that on average hosts one satellite galaxy. In other words, the average occupation number of satellite galaxies follows a power law proportional to $\langle N_{\rm Sat}\rangle \propto (M_{\rm halo}/M_1)^{\alpha}$. The solid green line in figure 6 is the average occupation number of both central and satellite galaxies: $\langle N_{\rm All}\rangle \equiv \langle N_{\rm Cen}\rangle + \langle N_{\rm Sat}\rangle$. For low halo masses, $\langle N_{\rm All}\rangle$ is closely related to $\langle N_{\rm Cen}\rangle$; however, for higher $M_{\rm halo}$, as the occupation number of satellite galaxies increases, $\langle N_{\rm All}\rangle$ is dominated by $\langle N_{\rm Sat}\rangle$.

Function	A	B	C
$\alpha = A + B({\rm z}+1-C)^2$	0.84(2)	0.003(1)	5.4(1.3)
$M_1 = A + Be^{-C({\rm z}+1)}$	0.2(1)	2.4(2)	0.34(3)

Table 3. Best fits for the evolution of the power law index α and normalization mass M_1 for increasing redshift.

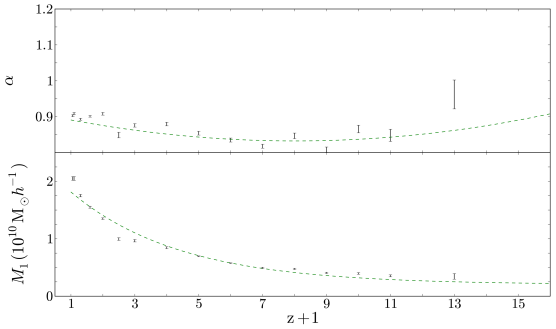

Figure 7. Summary plot of the best fit parameters α and M_1 as a function of redshift. The green curves are the best fits through each. Table 3 shows the fit functions used and the best fit parameters through these fits.

In order to fit the halo occupation number, we consider a function that is a combination of $\langle N_{\rm Cen}\rangle$ and $\langle N_{\rm Sat}\rangle$. Because the occupation number will be zero if $N_{\rm Cen} = 0$, we only fit halos that host a central galaxy; additionally, the fit function must have a power-law tail for large $M_{\rm halo}$. Therefore, we used a fit function of the form:

$$\langle N(M_{\rm halo})\rangle = 1 + (M_{\rm halo}/M_1)^{\alpha} \quad (7)$$

where M_1 is defined by $N_{\rm Sat}(M_1) = 1$, and α is the power-law index of the distribution. These fits are shown as the blue dot-dash curves on figure 6. The two fit parameters α and M_1 exhibit an evolution with redshift, which is shown in figure 7. The bottom panel of figure 7 shows the evolution of the normalization mass M_1, which exhibits a clear exponential decay with increasing redshift. The green dashed line is the best fit curve, and the fitting parameters and function are given in Table 3. In the top panel of figure 7 is the evolution of the slope of the power-law tail α. There seems to be a slight parabolic evolution with redshift for α, which is fitted as the green dashed curve; however, this evolution is very slight and may just be an artifact of the simulation. Nevertheless, the fit function along with the best fit parameters for α are also shown in Table 3

With the best fit functions given in Table 3, one could determine the normalization mass M_1 and power law index α at a given redshift, then use Eq. 7 to determine $\langle N\rangle$ in order to populate a given halo of mass $M_{\rm halo}$ for a simulation. However, in order to fully populate said halos, one must also understand the spread of the sub halo population at a certain value of $\langle N\rangle$. The best technique for this analysis is to compare the probability distribution of sub halos N at a given average occupation number $\langle N\rangle$, $P(N|\langle N\rangle)$, with that of a well defined probability distribution, more specifically

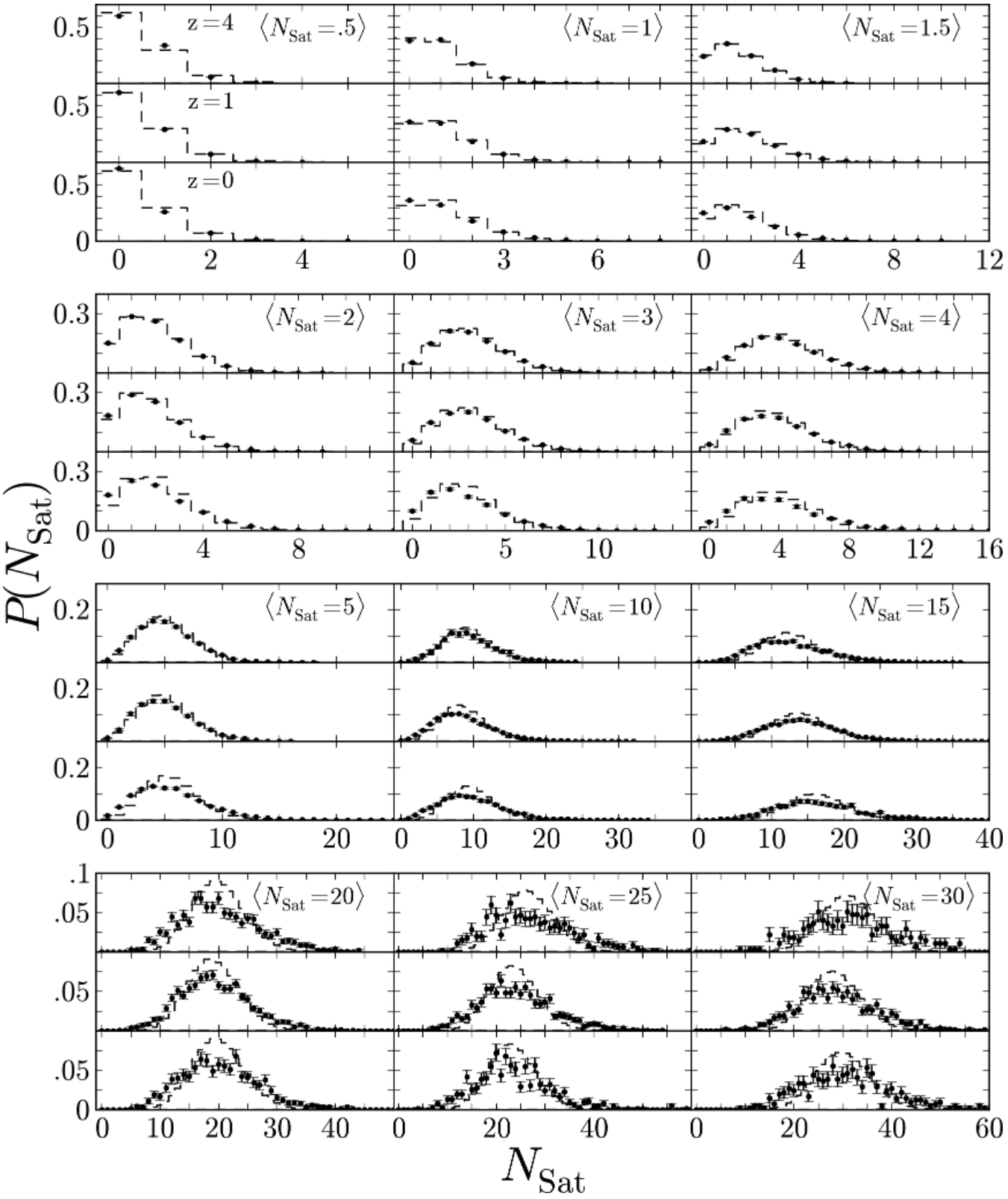

Figure 8. Probability distribution $P(N_{\rm Sat}|\langle N_{\rm Sat}\rangle)$ for a halo with virial mass $M_{\rm halo}$ and an average occupation number of $\langle N_{\rm Sat}(M_{\rm halo})\rangle$ will host $N_{\rm Sat}$ galaxies. Each plot is the distribution about a different value for $\langle N_{\rm Sat}\rangle$ which is given in the top right, while the three panels correspond to the three redshifts given in the first plot. The error bars shown are Poisson error bars. For comparison the dotted histogram is the corresponding Poisson distribution centered about $N_{\rm Sat}$. Each of the distributions can be very accurately approximated as a Poisson distribution.

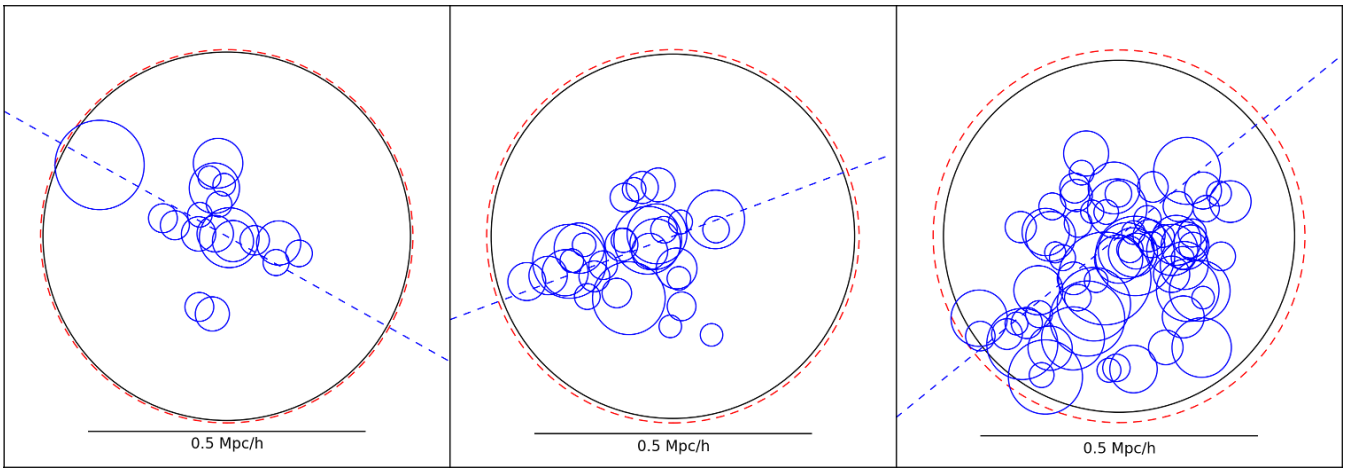

Figure 9. Plotted here is a simplistic schematic of the distribution of sub halos within three groups of mass $M_{\rm halo} \sim 10^{12} M_{\odot} h^{-1}$. The left panel shows a group with the fewest number of subhalos from our simulation, the center panel shows a group with an occupation number equal to $\langle N_{\rm Sat} \rangle$ given by Eq. 7, and the right panel shows a group with the largest number of subhalos from our distribution. The red dotted circles map out R_{Vir} of the parent halo, while the black and blue circles show R_{Vir} of the central and satellite subhalos, respectively. Subhalos are believed to live upon filamentary structures within groups so the blue dotted line roughly shows the filaments of each group.

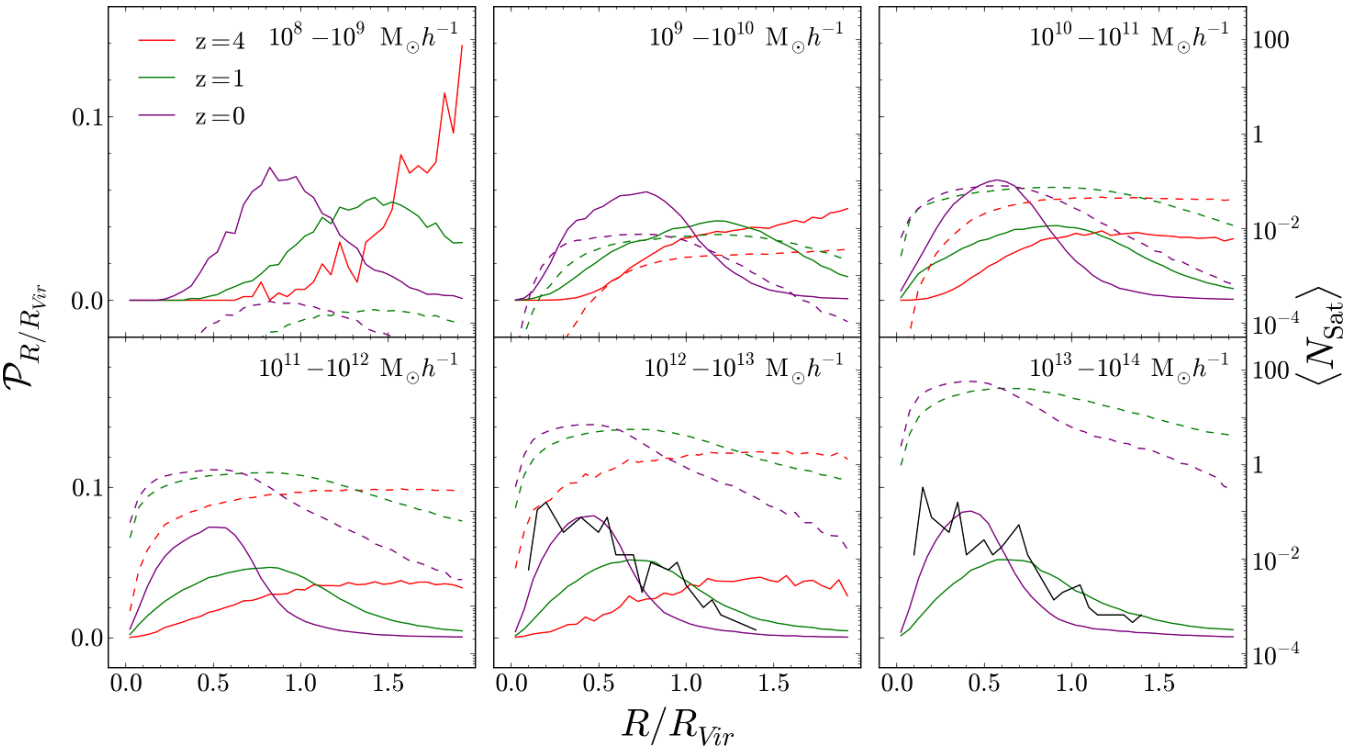

Figure 10. The solid curves here are the probability distribution $\mathcal{P}_{R/R_{Vir}}$ that a satellite subhalo will be located at a radial distance R from the center of the parent halo in units of the parent halo's R_{Vir}. Each panel corresponds to a parent halo mass bin which is given in the right hand corner of each panel. The colors of the curves correspond to a specific redshift which is given in the top left corner of the first (top left) panel. The dotted curves correspond to the occupation number $\langle N_{\rm Sat} \rangle$ at a certain radial distance from the center of the parent halo. In the last two panels, the black curves show the SPH results from Berlind et al. (2003).

a Poisson distribution (e.g. Zheng et al. (2005); Berlind et al. (2003)). If $P(N|\langle N \rangle)$ follows that of a Poisson distribution, then one could use Poisson statistics to quantize the spread of occupation number from the mean. The top panels of figure 6 show the width of the distribution; for a Poisson distribution the width is $\langle N(N-1) \rangle = \langle N \rangle^2$ which is shown as the dotted line at unity. The solid circles show the width of the probability distribution as a function of $M_{\rm halo}$ for all galaxies (both central and satellite). At all redshifts, this distribution is sub Poisson for low values of $M_{\rm halo}$, however, it quickly approaches Poissonian at larger $M_{\rm halo}$. Because the number of central galaxies follows a step function, there

is very little spread in this value, i.e. it is either 0 or 1, so instead of exploring the probability for all sub halos we focused on the probability distribution of satellite sub halos $P(N_{\rm Sat}|\langle N_{\rm Sat}\rangle)$. The open circles in the top panels of figure 6 show the width of the probability distribution as a function of $M_{\rm halo}$. Again for low halo masses, $P(N_{\rm Sat})$ is sub Poisson, but approaches a Poissonian width for higher masses. On the other hand, for extremely high halo masses at low redshifts, $P(N_{\rm Sat})$ again is sub Poisson. From the width of the distribution, it appears that $P(N_{\rm Sat})$ is very close to a Poisson distribution. In figure 8 we plotted $P(N_{\rm Sat}|\langle N_{\rm Sat}\rangle)$ for three different snapshots. Each plot shows the probability that a halo $M_{\rm halo}$ will host $N_{\rm Sat}$ satellite galaxies if on average the halo occupation number is $\langle N_{\rm Sat}(M_{\rm halo})\rangle$. In figure 8 the error bars are Poisson error bars and the dotted histogram is the Poisson distribution centered at $\langle N_{\rm Sat}\rangle$ which is given in the top right of each set of plots. From figure 8 and the top panels of figure 6, it is clear that $P(N_{\rm Sat}|\langle N_{S}at\rangle)$ can be approximated as a Poisson distribution; therefore, one can adequately use Poisson statistics to quantify the spread of sub halos from the best fit mean of Eq. 7

Now that we understand the mean occupation number for a halo at a certain redshift, we must also analyze the relative spatial distribution of the sub halos within their parent halo. As we discussed above, all sub halos can be classified as either central or satellite; furthermore, each halo will host either one or none central sub halos, so studying the relative spatial distribution of a central sub halo is a bit trivial, i.e. if the halo hosts a central sub halo it will be located in the center of the halo. Therefore, we will focus on analyzing the spatial distribution of only satellite sub halos. Figure 9 shows a simplified 2-D schematic of three different halos of mass $M_{\rm halo} \sim 10^{12}$ M$_\odot h^{-1}$ at z = 0 which is comparable to the Milky Way. The middle panel shows a halo with an occupation number equal to the mean at $M_{\rm halo}$ (see Eq. 7), while the left and right panels show, respectively, the halos with the minimum and maximum occupation number at $M_{\rm halo}$. The red dotted circle shows the virial radius of the parent halo, the black solid circle shows the virial radius of the central sub halo, and the blue circles show the satellite sub halos. Because the virial radius of a galaxy is depended on the mass of the galaxy, the size of the circle also represents the mass of each galaxy. This simplified representation easily shows the distribution of mass within each halo: the majority of the mass is located in one large sub halo located at the center of the group with many less massive galaxies scattered around the central sub halo. Furthermore, this simple schematic shows that the sub halos prefer to populate their parents halos along filaments which is roughly shown as the blue dotted line in figure 9.

In figure 10 we have plotted (*solid curves*) the probability density $\mathcal{P}_{R/R_{Vir}}$ that a satellite sub halo will be located a radial distance R from the the center of the group in units of the halo's R_{fir}. We chose to only investigate satellite galaxies here because we have already shown that halos can only host one central galaxy which would lead to a trivial analysis. We plotted halos from three different snapshots while each panel corresponds to different parent halo mass bins. In the last two panels (the high mass panels), there a no halos with mass $10^{12} < M_{\rm halo} < 10^{14}$ at z = 4, so there is no data from that snapshot plotted in these panels. For completeness, plotted on the right hand axes are the corresponding dotted curves of $\langle N_{\rm Sat}\rangle$ as a function of radial distance scaled by R_{200} for each snapshot. Here, $\langle N_{\rm Sat}\rangle$ is the average number of satellite sub halos per group per radial bin. In other words this value corresponds to the average number of satellite sub halos within a group *at* a certain radial distance R, which is *not* the average number of satellite sub halos *within* R. Also plotted as the the black curve plotted in the last two panels are SPH data from Berlind et al. (2003). Our distribution follows the same general form as Berlind et al. (2003). As can be seen in figure 10 the peak and width of the radial distribution of satellite galaxies decreases with decreasing redshift, irrespective of the mass of the parent halo. This suggests that with time satellite galaxies cluster strongly around the central galaxy and that mergers dominate over the accretion of new satellites. Additionally we see a mild variation for the peak of the distribution with the mass of the host halo at a given redshift. The relative location of the peak (with respect to $R_{\rm vir}$) decreases with increasing halo mass which suggests that the clustering of satellite galaxies is stronger in more massive halos.

6 GALAXY CLUSTERING

The MBII simulation is of a large enough volume that galaxy clustering can be studied meaningfully. The sheer number of galaxies in the MBII (particularly for low mass selection thresholds) means that clustering measures can be computed with a high signal to noise level and consequently subtle features be noticed and analyzed. In this section we concentrate on two-point correlation functions of the galaxies and dark matter, including the cross-correlation of the two.

6.1 Two point correlation functions

We analyze 15 snapshots of the simulation between redshifts $z = 10$ and $z = 0.06$. For each snapshot, we compute the two point autocorrelation of dark matter particles and also the two point autocorrelation function of subhalos. For the latter, we measure this quantity for several subsamples defined by a lower limit on the subhalo mass: $m_{\rm tot} > 10^9 M_\odot, 10^{10} M_\odot, 10^{11} M_\odot, 10^{12} M_\odot$. We also do the same for subsamples defined by lower limits on the stellar mass of subhalos: $m_* > 10^8 M_\odot, 10^9 M_\odot, 10^{10} M_\odot, 10^{11} M_\odot$. We also compute the cross-correlation of dark matter and subhalos for subsamples defined by the above mass bins.

We note that before computing the correlation functions for any sample in the simulation, if the number of elements (dark matter particles or subhalos) is greater than 256^3, for speed we randomly subsample down to this number, as shot noise errors on the scales we are interested in will be negligible at the sampling density.

In Figure 11, we show examples of the autocorrelations and crosscorrelations for galaxies and dark matter in the MBII at two redshifts, $z = 0$ and $z = 2$. In this example, the galaxies used to compute the clustering were selected above a total mass threshold of $10^9 M_\odot$. There were 1.65×10^6 galaxies in the subsample at $z = 0$ and 1.89×10^6 at $z = 2$. In Figure 11 we can see that the dark matter autocorrelation (referred to as $\xi_{\rho\rho}$ although it is not the autocorrelation of the total density) at $z = 0$ has the pronounced dip at

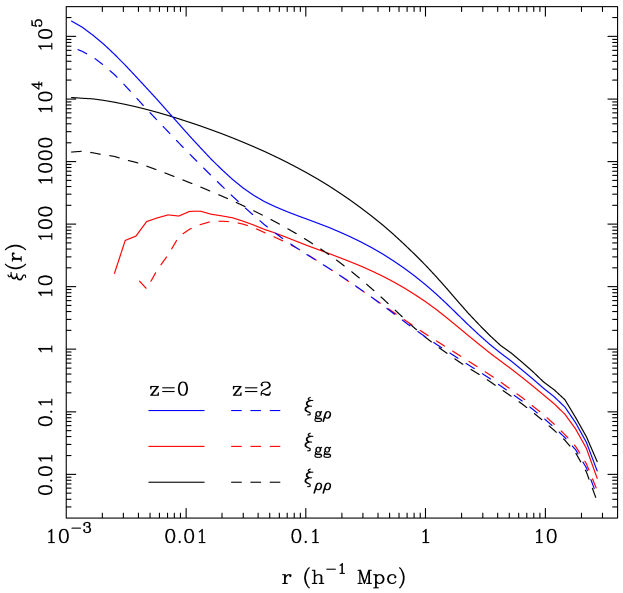

Figure 11. The two-point auto-correlation function of dark matter (black), galaxies (red) and the two-point cross-correlation function of dark matter and galaxies (blue) in the MBII simulation. We show results at two redshifts $z = 0$ and $z = 2$. The galaxies were selected to be those above a (total) mass threshold of $10^9 M_\odot$.

$r \sim 1\mathrm{h}^1\mathrm{Mpc}$ indicating the transition between one-halo and two-halo terms (Cooray & Sheth 2002). At redshift $z = 2$, the autocorrelation of galaxies and of dark matter particles have similar shapes and ampitudes on scales $r > 20\mathrm{kpc/h}$, but at $z = 0$ the galaxies (which have low mass) are significantly anti-biased with respect to the dark matter on all scales (see e.g., Abbas & Sheth 2007). The cross-correlation, $\xi_{g\rho}$ has a second dip in it at $r \sim 20\mathrm{kpc/h}$. The galaxies at the two redshifts have pretty similar $\xi_{g\rho}$ (dark matter profiles) interior to this, as expected, because they were selected above the same threshold mass.

6.2 Bias and stochasticity in MBII

6.2.1 Bias

That the ratio of dark matter and galaxy correlation functions can vary as a function of scale is obvious from Figure 11. In Figure 12 we plot $b(r) = \sqrt{\xi_{gg}(r)/\xi_{\rho\rho}}$ for the same lower total mass threshold $10^9 M_\odot$ as was used in Figure 11, but for redshifts between $z \sim 0$ and $z \sim 10$. The $b(r)$ function is approximately flat for separations $r > 2 - 5\mathrm{h}^1\mathrm{Mpc}$, depending on the redshift, reaching the limit on large scales usually referred to as linear bias (see e.g., Scherrer & Weinberg 1998). On smaller scales, the bias is scale-dependent, with bias decreasing as r becomes smaller for redshifts $z < 4$ and increasing for redshifts $z > 4$. For the mass threshold plotted, bias is approximately scale independent at $z = 4$ down to $r \sim 0.1\mathrm{h}^1\mathrm{Mpc}$. The scale dependence at late times is presumably due at least partly to non-linear effects such as merging of galaxies reducing the number of pairs on small scales, as well as halo exclusion. In the halo model framework, bias is scale dependent with a change of slope at the transition scale between the one and the two halo terms. At

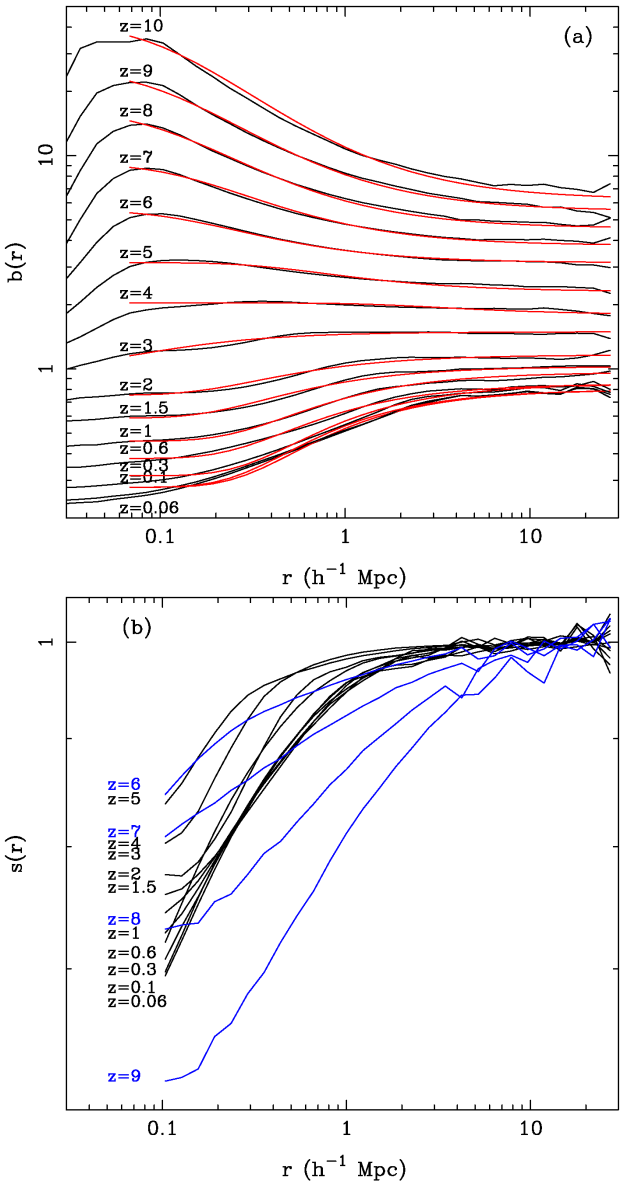

Figure 12. (a) *Top panel*: Bias vs scale for galaxies in the MBII simulation, at 15 different redshifts. The lower threshold mass of the MBII galaxy sample was chosen to be $10^9 M_\odot$. The simulation results are shown as solid black lines, and a simple parametric fit (Equation 8) to the results for each redshift is plotted as a solid red line. (b) *Bottom panel*: Stochasticity of galaxy clustering (Equation 10) as a function of scale for MBII galaxies. The same threshold mass ($10^9 M_\odot$) was used as in the top panel and the same redshift snapshots. In order to make the redshift progression clearer, we plot results at redshifts above $z = 5$ with blue lines and the low redshift results in black.

earlier times, because we are using a fixed threshold mass, the galaxies become rarer and so are likely to lie in primary halos (i.e. they are not in subhalos of larger halos).

In order to further see how this trend evolves, we have plotted in Figure 13 a simple fitting function for $b(r)$:

$$b_{\rm fit}(r) = (b_{\rm large} - b_{\rm small})e^{-(r_b/r)} + b_{\rm small} \qquad (8)$$

where $b_{\rm large}$ and $b_{\rm small}$ are fitting parameters corre-

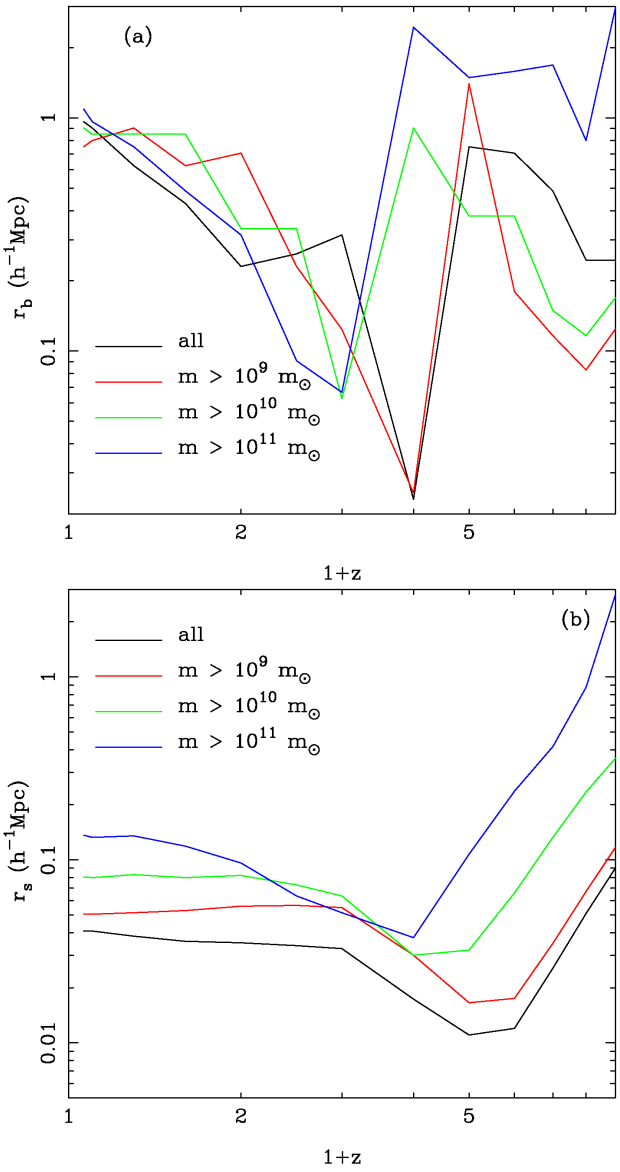

Figure 13. (a)Top panel: The non-linear scale in the bias (parameter r_b in Equation 8) of MBII galaxies as a function of redshift. We show results for four different lower mass thresholds as different colored lines. (b) Bottom panel: The non-linear scale in the stochasticity (parameter r_s in Equation 10) of MBII galaxies as a function of redshift. We show results for the same four different lower mass thresholds as the top panel.

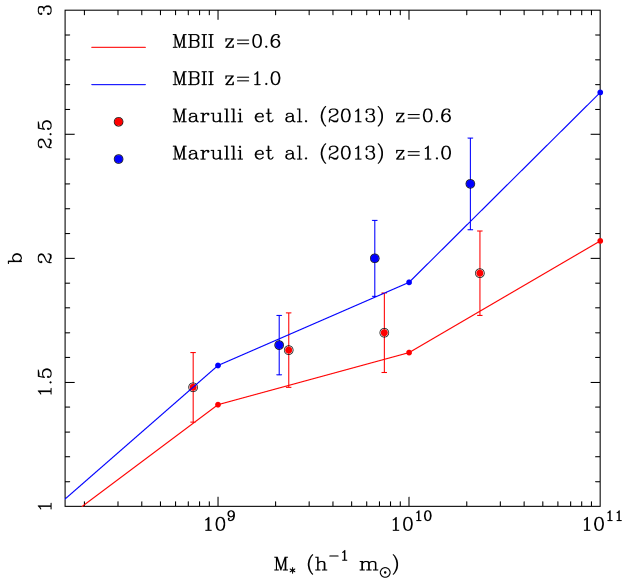

Figure 14. Top panel: Linear bias versus threshold galaxy stellar mass. Results for galaxies in the VIPERS survey (Marulli et al. 2013), are shown as points with error bars, at two different redshifts, $z = 0.6$ and $z = 1$. We show results from the MBII simulation at the same redshifts as solid lines.

sponding to the large-scale asymptote of the bias parameter and a value of bias on small scales, respectively. The parameter r_b corresponds to the exponential length scale over which the bias changes from its large to small scale value. This parameter r_b can therefore be considered to represent a type of non-linear scale parameter for the bias. We fit this function to the $b(r)$ curves for points with $r > 0.25\mathrm{h}^1\mathrm{Mpc}$, so that we avoid the downturn of $b(r)$ on small scales. The corresponding fits are shown as red lines in Figure 12(a).

We note that in Figure 12(a) that for the subhalo mass sample we are plotting the values of $b_{\rm large}$ and $b_{\rm small}$ in the fits will change relative to one another as we change redshift. As a result there will be a redshift (for this mass subsample it is around redshift $z = 3-4$) where the bias will be almost linear ($b_{\rm large} \simeq b_{\rm small}$). There is also likely to be a transition in the non-linear scale parameter r_b at around this redshift.

In Figure 13(a) we plot the behavior of r_b vs redshift, with results for several different mass bins on the same plot. At low redshifts $z < 2$ we can see a gradual increase in r_b with scale for all mass subsamples. This non-linear scale reaches a maximum of $1h^{-1}$Mpc at $z = 0$. This can be compared to the scale at which matter clustering becomes non-linear (the matter clustering deviates from the linear extrapolation), which is $\sim 5h^{-1}$Mpc at this redshift (Gaztañaga & Juszkiewicz 2001). Galaxies therefore trace the mass to scales significantly smaller than the non-linear mass clustering scale in this simulation.

The minimum value for r_b is reached at redshift $z = 2$ and is between $r_b = 0.01 - 0.05h^{-1}$Mpc with the smaller halos being at the lower end of this range. At earlier redshifts there is then a switch to a much larger value for r_b.

6.2.2 Stochasticity

Another quantity of interest is the stochasticity of clustering for which we use the correlation coefficient (see e.g., Sato & Matsubara 2013, we use the symbol $s(r)$ in order to avoid confusion with length scale r.)

$$s(r) = \xi_{g\rho}/\sqrt{\xi_{gg}\xi_{\rho\rho}} \qquad (9)$$

We show the $s(r)$ curves for the same redshifts and lower mass threshold ($10^9 M_\odot$) as used for Figure 13(a) in Figure 13(b). On large scales, $r > 1 - 15\mathrm{h}^1\mathrm{Mpc}$, depending on the redshift, the $s(r)$ reaches unity, indicating that the galaxy and dark matter fluctuations trace each other deterministically. For clarity, we have not plotted the smallest scales ($r < 0.1\mathrm{h}^1\mathrm{Mpc}$) on this plot, but all curves eventually rise again and go above $s = 1$ (this can be seen in Figure 16 below). The $s(r)$ increases for the smallest r because galaxies

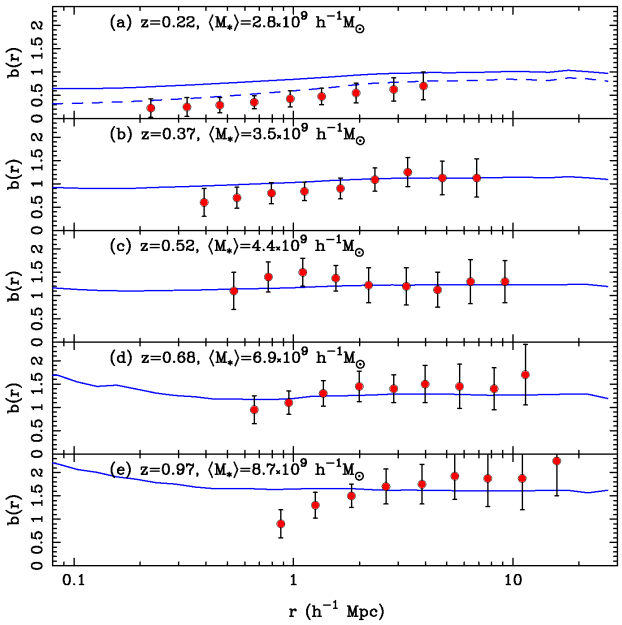

Figure 15. The scale dependence of bias in the MBII simulation (blue lines) compared to the observational data of Jullo et al. (2012) (points with error bars) for various samples with different mean stellar mass and redshift (given in the panels). The dashed line in panel (a) shows the results for an MBII sample with a mean stellar mass of $1.5 \times 10^9 M_\odot$.

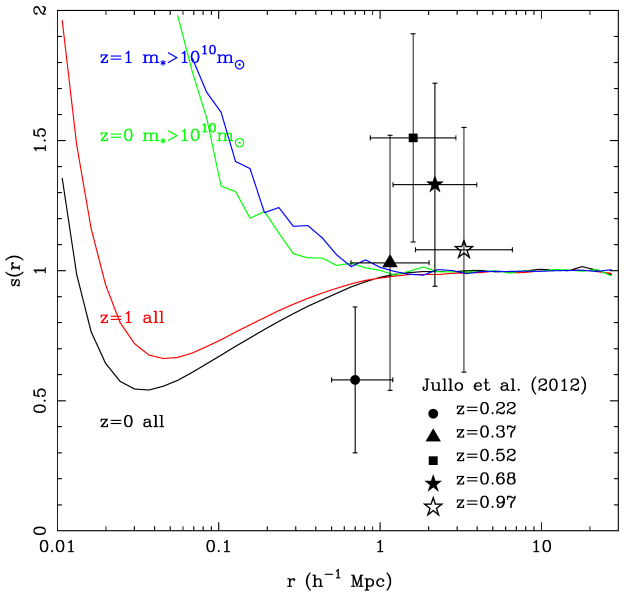

Figure 16. Stochasticity versus radius. Results for different redshifts and mass thresholds in the MBII simulation are shown as colored lines. The points with error bars denote observational determinations for galaxy stochasticity by Jullo et al. (2012). The simulation redshifts and mass bins shown bracket those of the observational data.

cannot be closer together than the sum of their radii. This causes ξ_{gg} in the denominator of Equation 9 to be very small (see e.g. Figure 11) and so $s(r)$ to increase.

Again in order to explore a wide range of masses and redshifts in one plot, we have fit a simple curve to the $s(r)$ results.

$$s_{\rm fit}(r) = e^{-(r_s/r)} \tag{10}$$

where r_s is a parameter which determines the scale at which the stochasticity $s(r)$ deviates from $s = 1$. The results for different mass bins are shown as a function of redshift in Figure 13(b). We can see that halos with larger masses have systematically higher values of r_s at almost all redshifts. Curves for all masses also have a trend of r_s with redshift which is somewhat similar to the r_b parameter in Figure 12. As the density field evolves below redshifts $z = 3 - 4$, the scale at which stochasticity becomes important increases. Unlike the bias parameter r_b it does appear to level off at the lowest redshifts, however.

6.3 Comparison with observations

We compare first to the galaxy autocorrelation function published by the VIMOS Public Extragalactic Redshift Survey (VIPERS) team (Marulli et al. 2013). The VIPERS survey is an ongoing deep and well sampled spectroscopic survey of 100,000 galaxies in the redshift range $z = 0.5 - 1.2$ (see Guzzo et al. 2013 for details). We use two of the three redshift bin measurements published by Marulli et al. (2013), centered at $z = 0.6$ and $z = 1.0$. Marulli et al. (2013) give the linear bias parameter for each redshift in a series of bins in stellar mass threshold (their table 3). We plot these linear bias vs stellar mass points in Figure 14. Results from the simulation are shown as lines (b in this case is the parameter $b_{\rm large}$ fit using equation 8). From Figure 14 we can see that the simulation and observations show the expected trend of increasing bias with increasing galaxy stellar mass, and that the simulations are consistent with the observational results.

Observationally analyses such as Jullo et al. (2012) have been able to probe scale dependence of bias by comparing weak-lensing measurements of the matter distribution with galaxy clustering. In Figure 15 we show a quantitative comparison between the MBII simulation and the data from figure 11 of Jullo et al. (2012) The Jullo et al. (2012) measurements were for 5 different subsamples of observed galaxies with different mean stellar masses and mean redshifts. In order to match the mean stellar masses and redshifts of the Jullo et al. (2012) data samples we carried out a quadrilinear interpolation in log mass and in redshift between the correlation function results measured from the MBII simulation for different redshift snapshots and mass bins. The relevant redshifts and mean stellar masses for the different samples are given in the panels of Figure 15.

Looking at Figure 15 we can see that observed data does show a pronounced antibiasing ($b < 1$) of galaxies with respect to dark matter on small scales for many of the galaxy subsamples. For the lowest redshift subsample (top panel) this is particularly significant, given the small error bars. The MBII simulation data exhibits this trend also, for the bins with low mass and low redshift. The bias for the lowest redshift bin is systematically higher at all scales in the simulations compared to the observations, however. In order to show quantitatively how this relates to the mean stellar mass of the subsample, for this panel, (a), we have also plot-

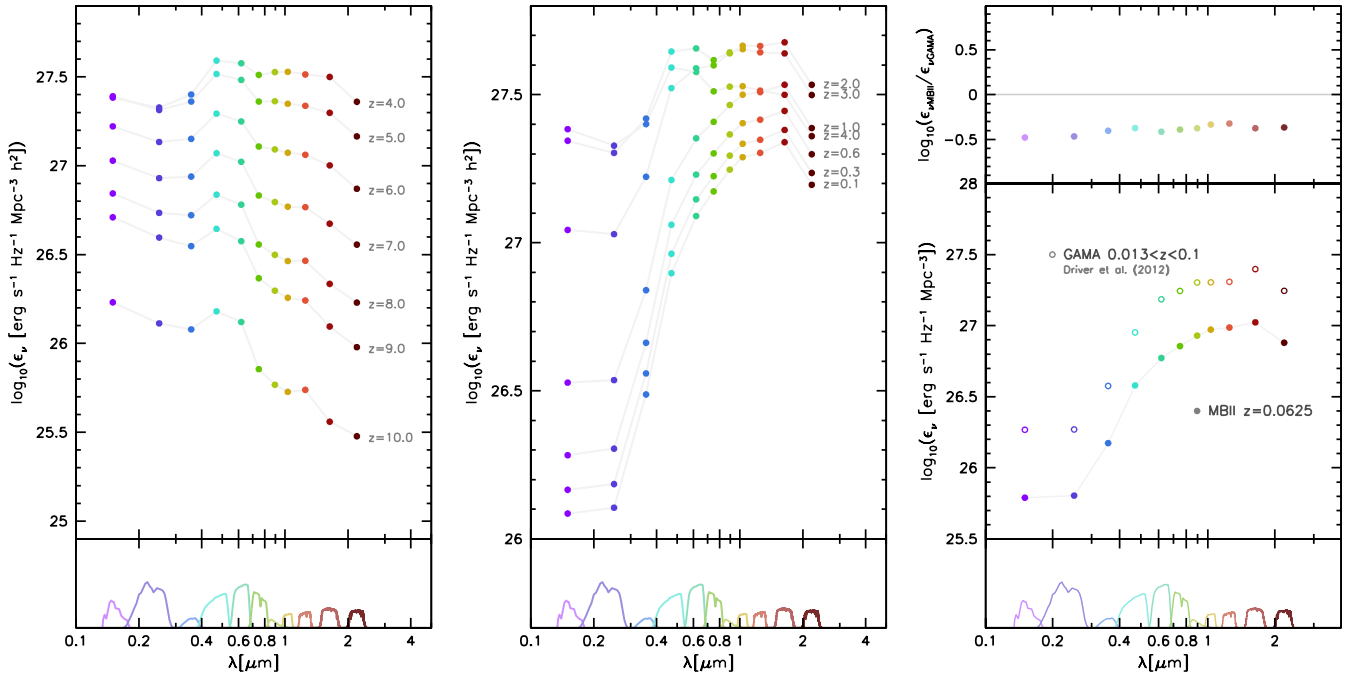

Figure 17. The Evolution of the Cosmic Spectral Energy Distribution in MBII (left and center panels. Comparison is made at $z = 0.0625$ with the GAMA survey at $z = 0.05$ Driver et al. (2012).

ted the results for a subsample with approximately half the mean stellar mass ($1.5 \times 10^9 M_\odot$).

Jullo et al. (2012) have also searched for for stochasticity in clustering by comparing weak-lensing measurements of the matter distribution with galaxy clustering. Jullo et al. (2012) find no significant amount of stochasticity on scales between $r = 0.2\mathrm{h}^1\mathrm{Mpc}$ and $r = 15\mathrm{h}^1\mathrm{Mpc}$ at redshifts between $z = 0.2$ and $z = 1$.

A comparison between the MBII simulation results and those of Jullo et al. (2012) is shown in Figure 16. The observational points are for a range of redshifts, with each redshift's measurement being reliably inferred over a particular range of scales (shown by the horizontal error bars). The different observational points also came from different flux limited samples, which have a mean stellar mass varying between $6 \times 10^9 M_\odot/\mathrm{h}$ and $1.8 \times 10^{10} M_\odot/\mathrm{h}$. We can see that the observational results are all consistent with no stochasticity ($s = 1$) at at least the 1.5σ level. The simulation results are shown for redshifts and stellar mass ranges which bracket the observational results. We can see that the observational and MBII results are consistent, but at the scales $r > 0.4\mathrm{h}^1\mathrm{Mpc}$ that are probed by Jullo et al. (2012) we expect no significant deviation from $s = 1$. On smaller scales for the MBII, we see differences between the two samples of different masses. The galaxy-exclusion effect mentioned above means that $s(r)$ goes above 1 at smaller scales for smaller galaxies.

7 PROPERTIES OF GALAXIES

The MB and MBII simulations have been very successful in reproducing the observed properties of galaxies in the high redshift Universe. Wilkins et al. (2013) showed that the galaxy stellar mass function (GSMF) predicted by MB and MBII at $z \geq 5$ could be reconciled with observations if one assumed that the mass-to-light ratio (as predicted in MB and MBII) of these galaxies was evolving with redshift. Khandai et al. (2012) showed that the MB simulation reproduced the observed properties of galaxies hosting the highest redshift quasars (Carilli et al. 2007; Wang et al. 2010, 2011). In this section we focus our attention on the properties of galaxies in the MBII simulation at $z < 4$. We will compare general properties of galaxies with observations and leave a detailed analysis to future publications.

We start by looking at the Cosmic Spectral Energy Distribution (CSED) in MBII. We select subhalos using SUBFIND and consider only those which have more than 100 dark matter particles. We refer to these subhalos as galaxies for the rest of this section. The spectral energy distribution (SED) of a galaxy is generated by summing the SEDs of each star particle in the galaxy. The left and right panels of figure 17 show the evolution of the CSED in the MBII simulation from $z = 10$ to $z = 0$. We find that the amplitude of CSED in all bands increases rapidly with decreasing redshift to $z = 4$ with little change in shape. This is expected and is in line with the behavior of the observed cosmic star formation rate (CSFR) (see figure 23). Observations find that the CSFR plateaus around $z \sim 3-4$ and declines rapidly at lower redshifts.

The shape of CSED evolves dramatically below $z \lesssim 3$. We find that the bluer part of the CSED, which strongly correlates with the CSFR starts to decline below $z \lesssim 3$ consistent with the observational trend, whereas the redder part of the CSED increases very slowly with decreasing redshift to $z \sim 1$ and declines thereafter. This is because at these

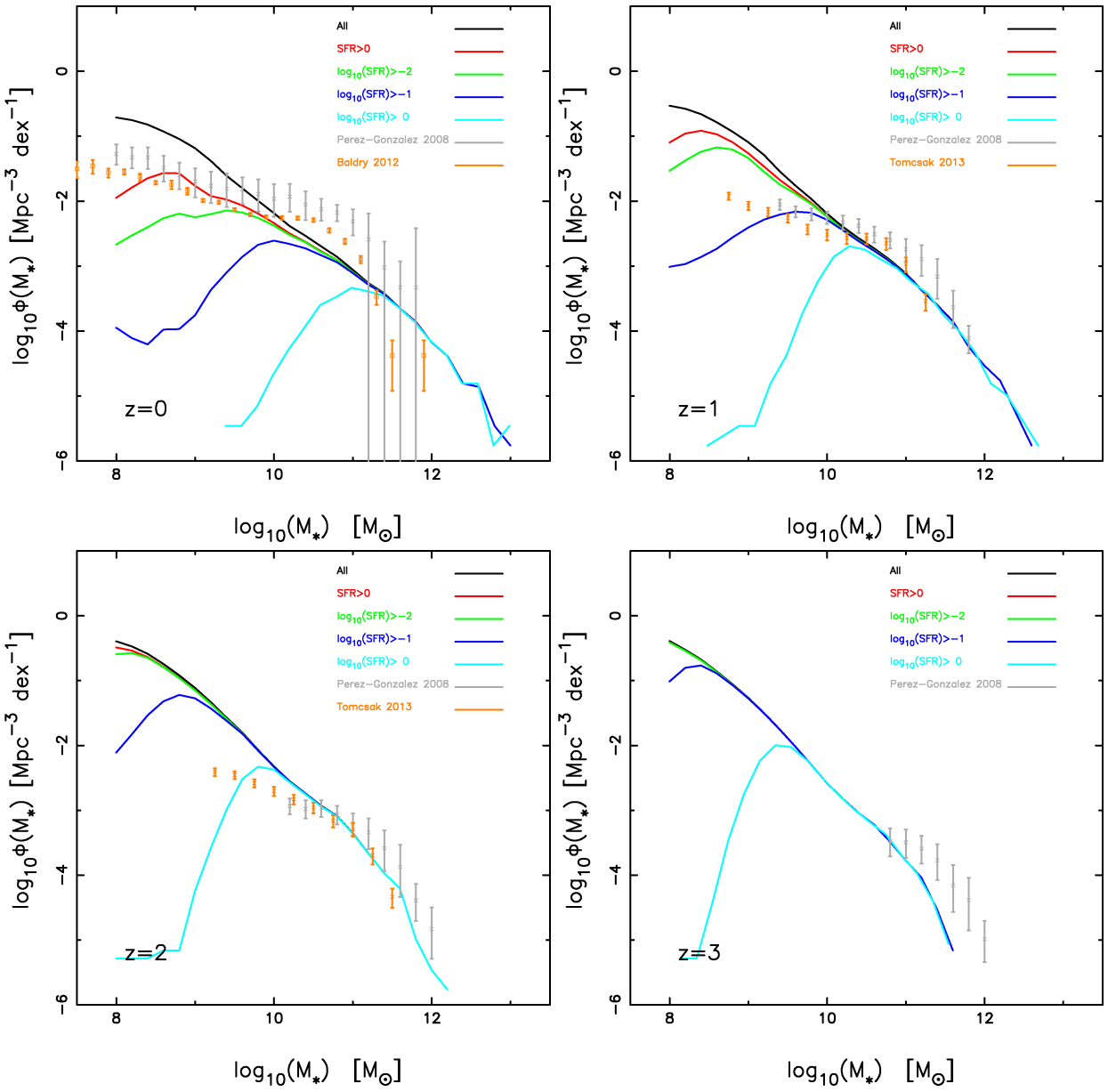

Figure 18. The GSMF from $z = 0 - 3$ in MBII. Comparison is made with observational estimates of Pérez-González et al. (2008) (gray data points with error bars), Baldry et al. (2012) (z=0, orange data points with error bars). For $z = 2$ and $z = 3$ (orange data points with error bars) the observational estimates are taken the CANDELS survey (Tomczak et al. 2013). The black line represents the GSMF in MBII when we consider all galaxies. The red, green, blue and cyan lines denote the population of galaxies which have a SFR greater than 0, 0.01, 0.1. and 1 respectively (in units of $M_\odot$/yr.)

redshifts galaxies are forming new stars at much reduced rates and are passively evolving into a redder population.

In the right-hand panel of figure 17 we compare the intrinsic CSED at $z = 0.0625$ with dust-corrected observations from the GAMA survey at $0.013 < z < 0.1$ (Driver et al. 2012). We find that the shape of the CSED compares well with the observational results. However, the amplitude of the CSED predicted by MBII does not match that of observations, falling systematically below it. This will be in part caused by incompleteness as MBII does not resolve all galaxies (particularly those at low stellar masses). This discrepancy is also sensitive to the initial mass function (IMF) assumed in the processing of MBII. Assuming an IMF in which a larger fraction of the mass is converted into high-mass stars (such as those proposed by Kroupa 2001; Chabrier 2003) would increase the luminosity density bringing MBII more closely inline with the observations

We now look at the galaxy stellar mass function (GSMF) predicted in MBII in figures 18 and 19. In figure 18 the GSMF is compared with observational estimates. The black line represents the GSMF in MBII when we consider all galaxies. The red, green, blue and cyan lines denote the population of galaxies which have a SFR greater than 0, 0.01, 0.1. and 1 respectively (in units of $M_\odot$/yr.) Comparison is made with observations of Pérez-González et al. (2008) (gray data points), Baldry et al. (2012) (orange data points

(z=0)). For $z = 2$ and $z = 3$ (orange data points) the observational estimates are taken the CANDELS survey (Tomczak et al. 2013). At $z = 0$ MBII overpredicts the GSMF both at the high and low mass ends. However the GSMF agrees well with the observations for $M_* \geq 10^{10} M_\odot$/h for $z = 1$ and $z = 2$ At $z = 3$ MBII underpredicts the abundance of larger mass galaxies. This is most likely due to the finite volume of MBII.

We find that the amplitude of the GSMF of (Hirschmann et al. 2013) is larger compared to MBII although the shape seems to be in reasonable agreement. The boxsize, star formation and feedback model in MBII and Hirschmann et al. (2013) are similar. Therefore given that the mass resolution of (Hirschmann et al. 2013) is $\sim \times 60$ lower than MBII and based on the resolution tests carried out in Torrey et al. (2014) the amplitude of the GSMF in (Hirschmann et al. 2013) should be lower compared to MBII.

One of the striking feature at all redshifts is the steep slope in the GSMF in MBII at $M_* \leq 10^{10} M_\odot$/h. These galaxies are less affected by AGN feedback and are therefore more sensitive to the star formation and stellar feedback model. This feature is seen across all redshifts in figure 18. For example in MBII we find that there are many more lower mass galaxies which have zero star formation (i.e. the difference between the black and red lines) at $z = 0$ as compared to higher redshifts, the difference between the two decreasing with increasing redshift. We therefore need to understand why do small galaxies form rapidly so early and why do they stop forming stars later. A better treatment of the star formation and stellar feedback model is therefore required in order to suppress the overproduction of lower mass galaxies. For example our model does not include the treatment of molecular gas (Krumholz & Gnedin 2011) which would tend to suppress star formation rates in lower mass galaxies. Alternately one may need to assume a feedback model which is dependent on the mass of the galaxy (Oppenheimer & Davé 2006; Davé et al. 2011; Vogelsberger et al 2013; Torrey et al. 2014). The variable wind model which is dependent on the galaxy velocity dispersion is described in Oppenheimer & Davé (2006) and indeed flattens the GSMF at $z = 0$ better reproducing observations. However Torrey et al. (2014) find that the GSMF is still steep at higher redshifts and additional modeling may be required to suppress the production of stars in low mass galaxies. Interestingly we find that if we account for those galaxies which have non-zero star formation at $z = 0$ the lower mass end of the GSMF is in better agreement with observations.

In figure 19 we look how the AGN population affects the GSMF at $z = 0$. We consider the the population of galaxies which may host an AGN with bolometric luminosity in units of erg/sec, $\log_{10}(L_{bol}) < 45$ (red), $\log_{10}(L_{bol}) < 43$ (green) and $\log_{10}(L_{bol}) < 41$ (blue) We focus our attention on larger mass galaxies at $z = 0$ since they are most affected by AGN feedback. We find that the tail of the GSMF is in reasonably good agreement with observations down to $z \geq 1$ (see figure 18) and one does not need to consider a subsample of galaxies without bright AGNs (green and blue curves) to match observations. We find that the stellar mass in galaxies that host AGNs brighter than $\log_{10}(L_{bol}) = 43$ is overpredicted in MBII suggesting insufficient quenching / AGN feedback. This is also seen in the results of Hirschmann et al. (2013). Torrey et al. (2014) on the other hand reproduce

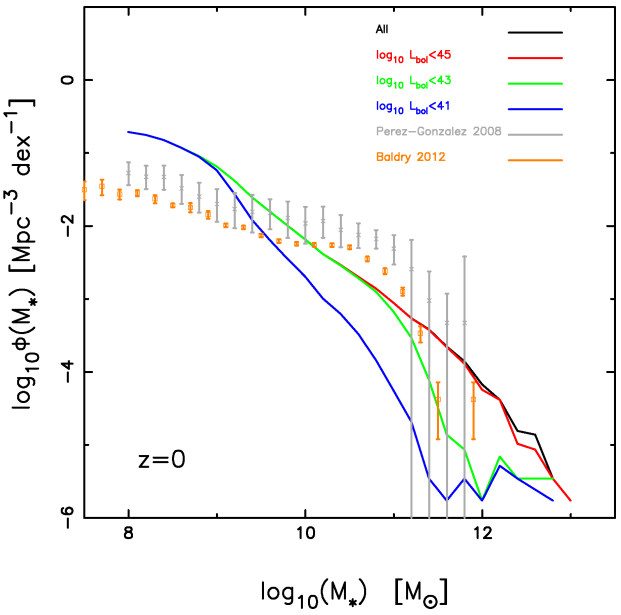

Figure 19. Same as in figure 18 but we now consider the the population of galaxies at $z = 0$ which may host an AGN with bolometric luminosity, $\log_{10}(L_{bol}) < 45$ (red), $\log_{10}(L_{bol}) < 43$ (green) and $\log_{10}(L_{bol}) < 41$ (blue).

the tail of the GSMF reasonably well although it maybe a result of missing cluster sized halos in their simulation volume of $L_{box} = 25$Mpc/h. Torrey et al. (2014) also define the galaxy stellar mass to be the sum of the stellar mass within twice the half mass radius. Such a definition affects only larger objects as it gets rid of the stellar mass in the diffuse intracluster medium and is not traditionally counted as contributing to the central galaxy's mass. Such a definition may help in better bringing in line our results with observations but as we will discuss in the next section the bright end of the QLF is still overestimated due to insufficient AGN feedback.

8 BLACKHOLES

In this section we present some basic properties of our simulated black hole population and their relation to the galaxies in MBII. In particular we show overall history of the black hole mass assembly and look at the relation between black hole and stellar mass in galaxies. We look at the predictions for the bolometric luminosity function and clustering strength as a function of luminosity for the AGN population in MBII. More detailed analysis of the blackhole-galaxy relations and comparisons with observational constraints will be presented in a separate paper.

Every single black hole in our simulations accretes and grows according to local gas properties so as an outcome of our black hole model, each single black hole that has a lightcurve and an associated mass history over the cosmic time since it is seeded. MBII contains tens of thousands of blackholes and Figure 20, we show the mean (and associated dispersion, in the corresponding colored areas) blackhole mass assembly history for blackholes that, at $z = 0$, end up in different mass bins, from the the lowest masses

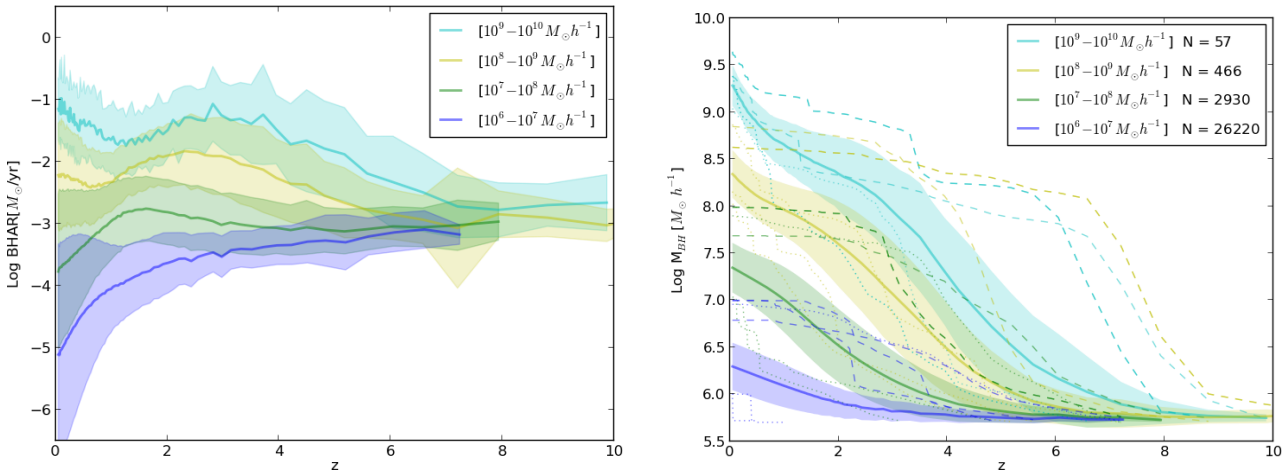

Figure 20. The mean black hole accretion rate (left panel) and the mean black hole mass assembly history for the main progenitor (right panel) black holes ending up in different mass ranges (as labeled) at $z = 0$. N indicates the number of black holes in each of the mass bins. The dashed and dotted lines show a sample of single main progenitor histories.

($10^6 M_\odot$/h $< M_{BH} < 10^7 M_\odot$/h) to the highest mass bin ($10^9 M_\odot$/h $< M_{BH}, 10^{10} M_\odot$/h). In addition to the mean histories for the population we also specifically show a sample of single, main progenitor mass assembly histories. This is to illustrate how the most massive, and earliest growing black holes, within the different mass bins, depart from the mean (dominated by the more numerous lower mass blackholes). In general we see that the largest black holes $z = 0$ are largely assembled at high redshifts. The dispersion in mass assembly histories is also typically larger for the high mass black holes. This is because there is a much larger variety of assembly histories than for the lower masses. For example, some black holes form early and grow to large masses quickly at high-z, but their mass assembly history remains flat subsequently. We also note an upturn in the growth histories of massive black hole at $z < 0.2$. This is likely the result of insufficient AGN feedback (in the form that is modeled in MBII) in massive galaxy hosts at low redshift. Similar results were also found by recent work of Hirschmann et al. (2013).

To illustrate the range of black hole masses and luminosities in MBII we show these two quantities as a function of total halo mass in our galaxies in Figure 21. Although there is an overall correlation between both quasar luminosity and black hole mass with halo mass the scatter in both these relations is rather large indicating the halo mass is an extremely rough proxy to black hole properties. Complex hydrodynamic and associated feedback effects play an important role in the central region of galaxies.

In Figure 22 we show the prediction for the relationship between black hole mass and stellar mass in galaxies in our simulation. In the right panel, the relation is shown for the $z = 0$ blackhole population. For simplicity here we use the total stellar mass and not only the bulge mass which is what is normally used in the local universe (and hence show only groups with $M_* > 10^{10} M_\odot$; in future work we will look at the associated black hole- stellar velocity dispersion relation). In the left panel of Figure 22 we show the evolution of the mean relation derived from a number of snapshots from MBII. As in previous work (Di Matteo et al. 2008; Booth & Schaye 2011; Hirschmann et al. 2013) we find good agreement between simulations and observations. Although we do not find strong evolution in the relation with redshift the relation appears to steepen slightly toward higher redshift. This is overall consistent with previous findings and observation constraints (Bennert et al. 2010; Merloni et al. 2010) and we defer detailed comparison with different observational constraints as a function of redshift to a future paper (Degraf et al. 2014).

The global star formation rate and black hole accretion rate density (multiplied by a factor of 3×10^3) is shown in Figure 23 together with the observational compilation of Hopkins & Beacom (2006) for the star formation rate density derived from different wavebands. Overall the star formation rate and black hole accretion rate density have similar shapes and track each, with the peak of star formation proceeding that of BHAR density by roughly a unit redshift. Both the star formation rate density (and also the BHAR density) show a flattening below $z \sim 1$. This is likely a result of too inefficient feedback to quench both SFR and BHAR in low redshift high mass halos.

In figure 24 we show the bolometric quasar luminosity function (QLF) compared to the compilation of data from Hopkins, Richards, & Hernquist (2007), at $z = 0.1, 0.5, 1, 1.5, 2$ and 4. We note that $z > 5$ predictions from MBII (and MB) are presented in DeGraf et al. (2012); McGreer et al. (2013) and predictions for $z = 2.0, 2.4, 3.2$ compared to the most up-to-date BOSS QLF in Ross et al. (2013). In general, we find overall good agreement between the simulations and observations at $z > 2$ (here and in DeGraf et al. (2012); McGreer et al. (2013); Ross et al. (2013) and $0.5 < z < 1$. At the lowest redshifts ($z = 0.1$), however, the bright end of the QLF is overestimated by the simulations. As we discussed earlier in the Section, this indicates insufficient quenching / AGN feedback at these redshifts. Conversely, in the redshift range between $z = 1.5 - 2$ the bright end of the QLF is underestimated (see also Ross et al. 2013). This would indicate that our peak of the BHAR density occurs somewhat too early (see Fig. 23). Again this may have to do with the details AGN feedback. Given the simple model adopted here, these results suggest that a constant f (our feedback energy parameter) may be too simplistic a model for AGN feedback. A redshift evolution of f as also implemented by Hirschmann et al. (2013) may alleviate

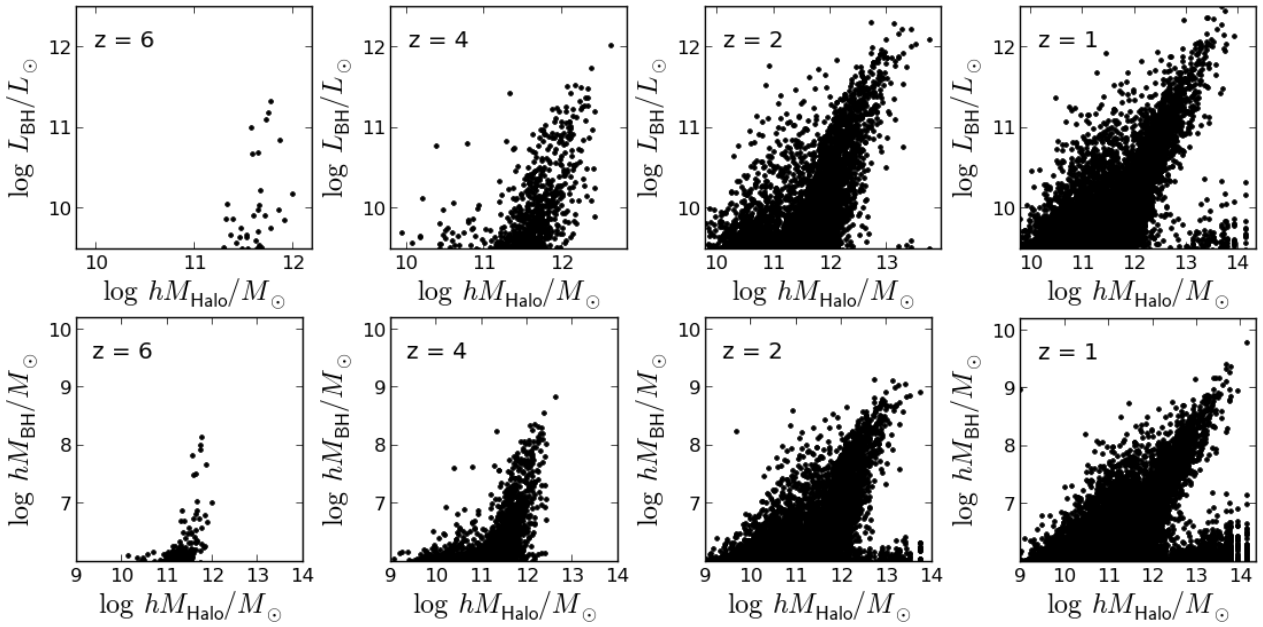

Figure 21. The relation between blackhole luminosity and host halo mass (top) and blackhole mass and host halo mass (bottom).

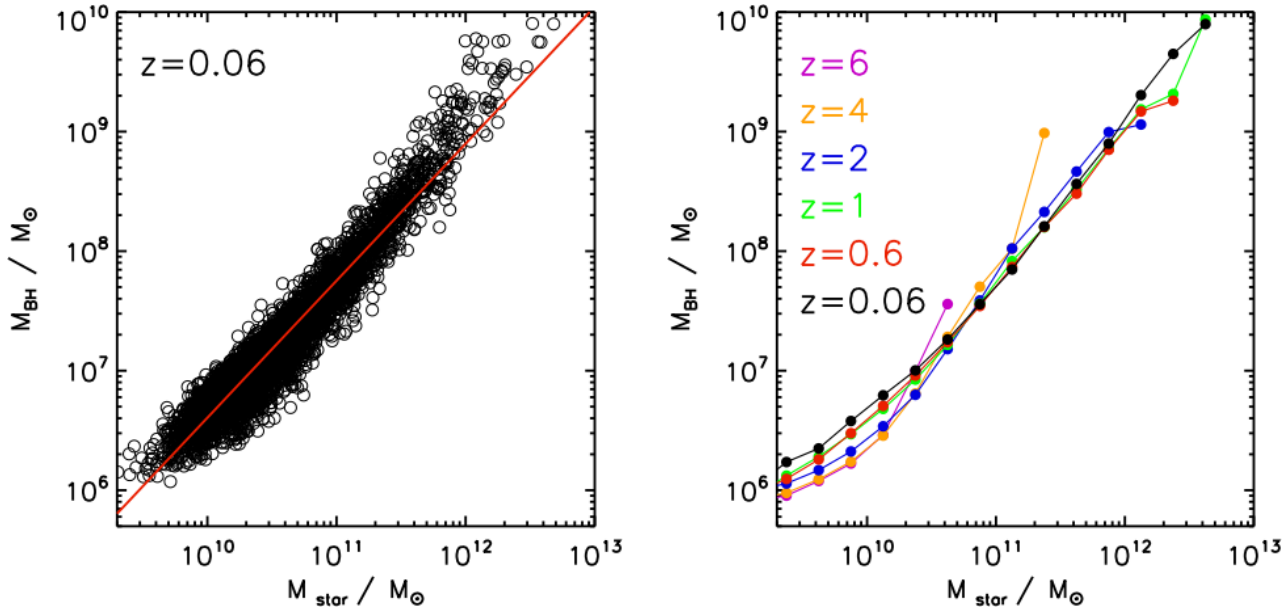

Figure 22. Left panel: present day blackhole mass stellar mass relation in MBII. Right panel: the evolution of the relation from $z = 0$ to $z = 6$.

some of these issues (however, even in those simulations the bright end (at low-z) is overestimated indicating that some more complicated modeling may be necessary).

Finally we briefly present the MBII prediction for the correlation length, r_0 of AGN as a function of redshift and luminosity in Figure 25. In general the correlation lengths are in agreement with observational constraints (Shen et al. 2009). The correlation length, at constant luminosity, increases as a function of redshift. This is expected if same luminosity AGN are hosted in similar mass halos at different redshifts. In addition, there is a luminosity dependence in the clustering and r_0 increases by a factor of $2-3$ at the highest luminosities.

9 CONCLUSIONS

In this paper we have examined a variety of standard predictions using the recently completed MBII simulation. In particular, the results presented here range from the clustering of halos and galaxies, HOD, the mass function of halos to basic properties of galaxies and AGNs.

Our main conclusions are:

- We find that halos with masses $M_{halo} \geq 10^{13} M_\odot/h$ have a baryon fraction close to 80%-90% of the cosmic mean. The baryon fraction decreases steadily with decreasing halo mass. Our results are broadly consistent with Crain et al. (2007) for cluster sized halos but differ significantly for lower mass halos. The discrepancy can be attributed to feedback

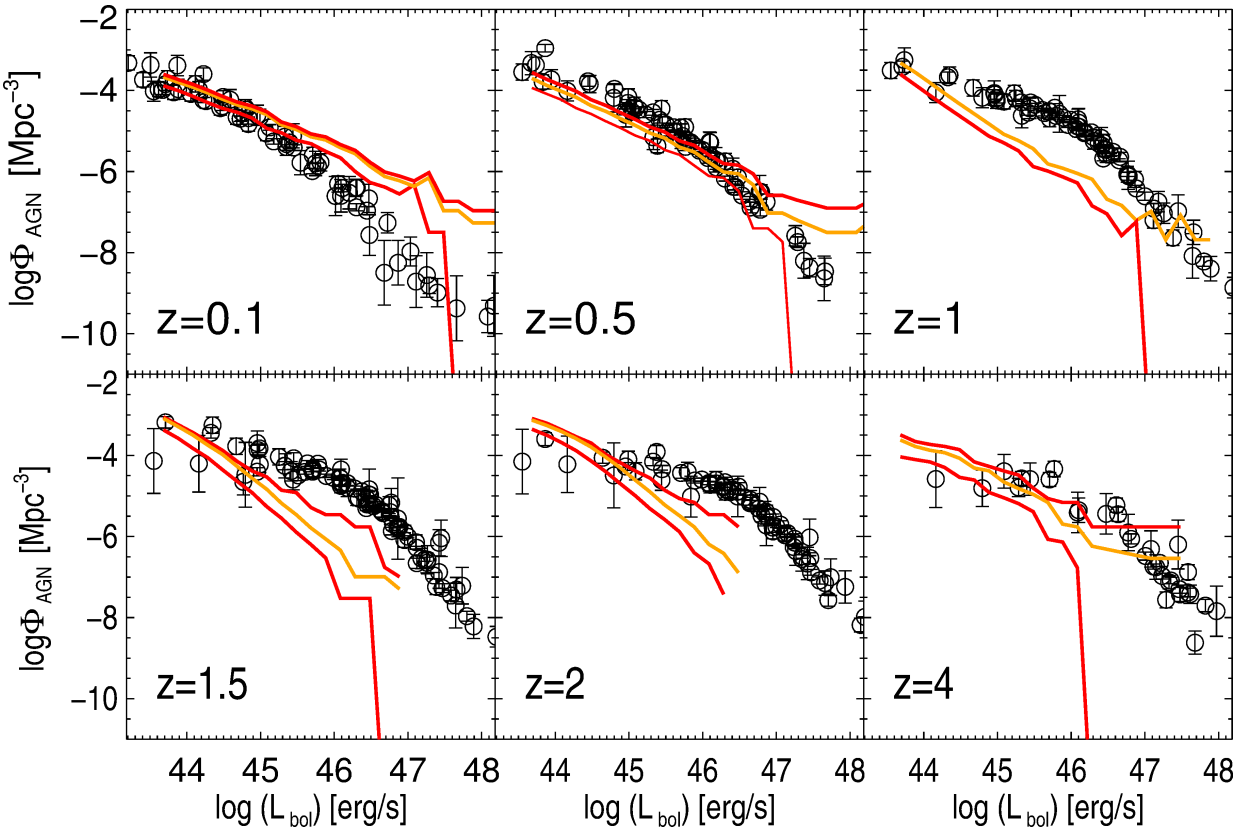

Figure 24. MBII Predictions for the quasar luminosity function (QLF) compared to the Hopkins, Richards, & Hernquist (2007) data compilation at different redshifts.

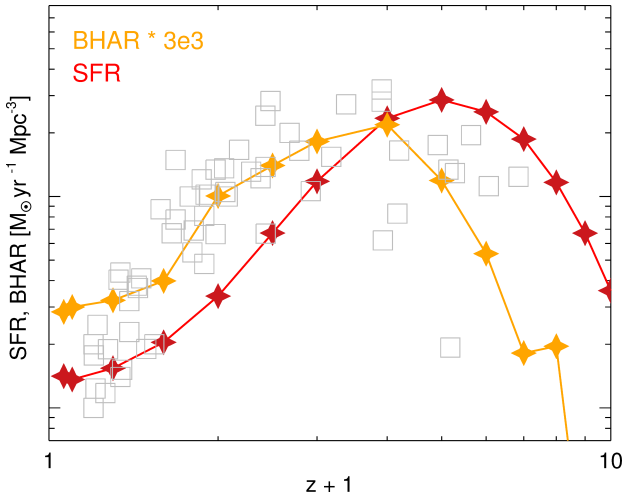

Figure 23. The star formation rate (SFR, in red) and black hole accretion rate (BHAR, in orange, multiplied by 3×10^3 for comparison) density prediction from MBII. The observation constraints for the SFR density from Hopkins & Beacom (2006) are shown in gray squares (without error bars for clarity).

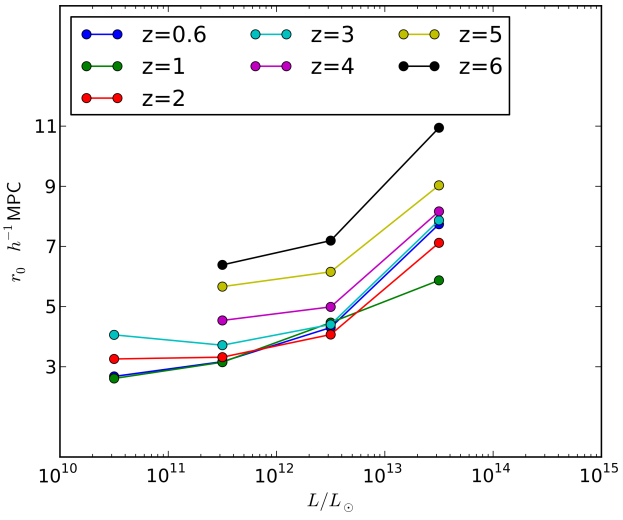

Figure 25. The correlation length, r_0 measured for the quasar population as a function of quasar luminosity plotted for different redshifts (as labeled).

both from AGN and supernovae which were not been modeled in Crain et al. (2007).

- We find that the FOF halo mass function (where halo mass includes both dark matter and baryonic components) in MBII can be fit with a universal form (valid for all redshifts) at the $\sim 13\%$ level.
- One of the most striking results predicted by MBII is the behavior of the halo mass function which shows a strong suppression in the abundance of halos below the knee of the mass function ($\ln(1/\sigma) \lesssim -0.2$ which corresponds to $M_{\rm halo} \sim 10^{13.2} M_\odot/{\rm h}$ at $z = 0$ and $M_{\rm halo} \sim 10^{9.5} M_\odot/{\rm h}$ at $z = 3$) when compared to dark matter only predictions of the halo mass function. This is due to the significant impact

of baryonic processes which tend to suppress the mass of the halo by up to 30% Sawala et al. (2013).

• Fits to the mass function from dark matter only simulations overpredict the mass function at the 20-35% level below the knee of the mass function at $\ln(1/\sigma) \lesssim 0.2$.

• We have quantified the scale dependence of bias and stochasticity in the simulation. We find that scale of the deviation from a linear fit for both bias and stochasticity reaches a minimum at $z \sim 3-4$. The galaxy and mass density field can in this sense be said to trace each other most closely at this redshift.

• The MBII overall matches most observed measurements of galaxy clustering with stellar mass. There are however some discrepancies in the bias at the lowest masses and redshifts probed. The simulation is consistent with observed measurements of stochasticity from combinations of galaxy clustering and weak lensing.

• We find that the HOD is well described by a power law behavior (see equation 7). We find a modest evolution for the power law slope however the normalization mass for the distribution exhibits an exponentially decaying behavior with redshift.

• The location of the peak and the width for the radial distribution of satellite galaxies decrease with decreasing redshift irrespective of the host mass of the halo, showing that satellite galaxies cluster more strongly around the central galaxy with time.

• We find that the shape of the CSED in MBII is consistent with observed data. The amplitude is however much lower and can be attributed to incompleteness at low galaxy masses in MBII.

• The GSMF predicted by MBII is consistent with observations out to $z = 2$. At lower redshifts however the MBII GSMF is much steeper at lower masses whereas MBII over produces stars at larger masses at $z = 0$.

• We find black hole mass and AGN luminosity to be broadly correlated to host $M_{\rm halo}$ but with very large scatter, indicating a wide range of black hole properties for a given halo mass. However, the local $M_{\rm BH} - M_*$ relation is tighter and consistent the observed one. Our results also imply very moderate evolution for the $M_{\rm BH} - M_*$ from $z \sim 2$. The global star formation rate density and black hole accretion rate density are also similar, but with a peak for the latter shifted to later times.

• The bolometric luminosity function of the simulated AGN population is broadly consistent with observational constraints (Ross et al. 2013, see also). We note however that simple thermal coupling for AGN feedback appears to quench the bright end of the AGN LF too fast around $z \sim 2$ whilst not being sufficient to fully quench the brightest AGN at $z = 0$. The best agreement with observations is at $z > 2$ and $z \sim 1$. Our results show a weak dependence of AGN clustering with luminosity. (Note that we defer to future work we to carry out detailed analysis of AGN population).

The MBII simulation is the largest simulation of its kind run to date with sufficient resolution to resolve $10^9 M_\odot$/h halos. We have found that the properties, such as HOD and clustering are consistent with previous work and observations. However we find that feedback from AGNs is still not sufficient at lower redshifts to properly account for the properties of large galaxies and AGNs since it is unable to quench star formation in massive galaxies and the abundance of luminous quasars. However it describes the current state of standard SPH simulations of galaxy formation and should be used as a testbed for improving models of galaxy formation. The parameters used in MBII were based on much smaller SPH simulations which missed these large halos in their volumes and thus could not find discrepancies with observations at the large mass end.

At smaller masses the GSMF in MBII is very steep compared to observational constraints. A variable wind model based on the galaxy velocity dispersion (Oppenheimer & Davé 2006; Davé et al. 2011; Vogelsberger et al 2013; Torrey et al. 2014) has been shown to flatten the GSMF at smaller masses to better reproduce observational constraints at $z = 0$. However at higher redshifts these models still predict a steep slope. On the other hand we find that AGN feedback is still insufficient to quench star formation in the most massive galaxies. The effect of AGNs is important in regulating the growth of massive galaxies; e.g. the results of Davé et al. (2011) (which do not include AGN feedback) and those of Vogelsberger et al (2013); Torrey et al. (2014) (which include AGN feedback) clearly illustrate how AGNs affect the stellar content of massive galaxies. However these simulations are still small in volume and miss out on massive halos. It would be interesting to see their predictions when run on boxes similar in size to MBII. In subsequent work we will look at improving on the feedback models employed in MBII.

One of the important effects we have quantified here is the effect of baryonic processes on the halo mass function. Although we find that the universality of the mass function in MBII holds at the 13% level consistent with previous work, we find considerable differences in the abundance of halos below the knee of the mass function when compared to dark matter simulations. One of the natural questions which arise are: how do different models for star formation, black hole growth and feedback affect the mass function? How strong is the redshift dependence? What can be said of halo abundance matching techniques and their predictions when done with mass functions such as MBII? These questions can only be addressed with simulations with different galaxy formation models and corresponding dark matter simulations which we will address in future work.

ACKNOWLEDGMENTS

The simulations were run on the Cray XT5 supercomputer Kraken at the National Institute for Computational Sciences. This research has been funded by the National Science Foundation (NSF) PetaApps programme, OCI-0749212 and by NSF AST-1009781. NK would like to aknowledge useful discussions with Michael Boylan-Kolchin and Erin Sheldon.

REFERENCES

Abbas U., Sheth R. K., 2007, MNRAS, 378, 641
Bagla J. S., Ray S., 2005, MNRAS, 358, 1076
Bagla J. S., Prasad J., 2006, MNRAS, 370, 993
Baldry, I. K., Driver, S. P., Loveday, J., et al. 2012, MNRAS, 421, 621

Battaglia N., Bond J. R., Pfrommer C., Sievers J. L., 2012, ApJ, 758, 74
Baugh C. M., 2006, RPPh, 69, 3101
Begelman M. C., Volonteri M., Rees M. J., 2006, MNRAS, 370, 289
Bennert, V. N., Treu, T., Woo, J.-H., et al. 2010, ApJ, 708, 1507
Berlind, A. A., & Weinberg, D. H. 2002, ApJ, 575, 587
Berlind, A. A., Weinberg, D. H., Benson, A. J., et al. 2003, ApJ, 593, 1
Bertschinger E., 1998, ARA&A, 36, 599
Bhattacharya, S., Heitmann, K., White, M., et al. 2011, ApJ, 732, 122
Booth C. M., Schaye J., 2009, MNRAS, 398, 53
Booth, C. M., & Schaye, J. 2011, MNRAS, 413, 1158
Boylan-Kolchin M., Springel V., White S. D. M., Jenkins A., Lemson G., 2009, MNRAS, 398, 1150
Bryan G. L., Norman M. L., 1997, ASPC, 123, 363
Carilli C. L., et al., 2007, ApJ, 666, L9
Cen R., 1992, ApJS, 78, 341
Chabrier, G. 2003, PASP, 115, 763
Chatterjee S., Degraf C., Richardson J., Zheng Z., Nagai D., Di Matteo T., 2012, MNRAS, 419, 2657
Colberg J. M., Di Matteo T., 2008, MNRAS, 387, 1163
Cooray, A., & Sheth, R. 2002, Physics Reports, 372, 1
Crain, R. A., Eke, V. R., Frenk, C. S., et al. 2007, MNRAS, 377, 41
Crain R. A., et al., 2009, MNRAS, 399, 1773
Crandall S., Ratra B., 2013, arXiv, arXiv:1311.0840
Croft R. A. C., Di Matteo T., Springel V., Hernquist L., 2009, MNRAS, 400, 43
Davé, R., Oppenheimer, B. D., & Finlator, K. 2011, MNRAS, 415, 11
Davis M., Efstathiou G., Frenk C. S., White S. D. M., 1985, ApJ, 292, 371
Degraf C., Di Matteo T., Springel V., 2010, MNRAS, 402, 1927
DeGraf C., Di Matteo T., Khandai N., Croft R., Lopez J., Springel V., 2012, MNRAS, 424, 1892
Degraf C., Oborski M., Di Matteo T., Chatterjee S., Nagai D., Richardson J., Zheng Z., 2011b, MNRAS, 416, 1591
Degraf C., Di Matteo T., Springel V., 2011, MNRAS, 413, 1383
Degraf, C. et al, 2014 (in preparation)
Di Matteo T., Khandai N., DeGraf C., Feng Y., Croft R. A. C., Lopez J., Springel V., 2012, ApJ, 745, L29
Di Matteo T., Springel V., Hernquist L., 2005, Natur, 433, 604
Di Matteo T., Colberg J., Springel V., Hernquist L., Sijacki D., 2008, ApJ, 676, 33
Dolag K., Borgani S., Schindler S., Diaferio A., Bykov A. M., 2008, SSRv, 134, 229
Driver, S. P., Robotham, A. S. G., Kelvin, L., et al. 2012, MNRAS, 427, 3244
Feng Y., et al., 2011, ApJS, 197, 18
Fioc M., Rocca-Volmerange B., 1997, A&A, 326, 950
Fioc M., Rocca-Volmerange B., 1999, astro, arXiv:astro-ph/9912179
Gaztañaga E., Juszkiewicz R., 2001, ApJ, 558, L1
Governato F., Willman B., Mayer L., Brooks A., Stinson G., Valenzuela O., Wadsley J., Quinn T., 2007, MNRAS, 374, 1479
Guzzo L., et al., 2013, arXiv, arXiv:1303.2623
Häring N., Rix H.-W., 2004, ApJ, 604, L89
Hinshaw G., et al., 2013, ApJS, 208, 19
Hirschmann M., Naab T., Somerville R. S., Burkert A., Oser L., 2012, MNRAS, 419, 3200
Hirschmann M., Dolag K., Saro A., Borgani S., Burkert A., 2013, arXiv, arXiv:1308.0333
Hopkins, A. M., & Beacom, J. F. 2006, ApJ, 651, 142
Hopkins P. F., Richards G. T., Hernquist L., 2007, ApJ, 654, 731
Jenkins, A., Frenk, C. S., White, S. D. M., et al. 2001, MNRAS, 321, 372
Jullo E., et al., 2012, ApJ, 750, 37
Katz N., White S. D. M., 1993, ApJ, 412, 455
Kennicutt R. C., Jr., 1989, ApJ, 344, 685
Khandai, N., Feng, Y., DeGraf, C., Di Matteo, T., & Croft, R. A. C. 2012, MNRAS, 423, 2397
Klypin A. A., Trujillo-Gomez S., Primack J., 2011, ApJ, 740, 102
Komatsu E., et al., 2011, ApJS, 192, 18
Kroupa, P. 2001, MNRAS, 322, 231
Krumholz M. R., Gnedin N. Y., 2011, ApJ, 729, 36
Lacey, C., & Cole, S. 1994, MNRAS, 271, 676
Lahav O., Liddle A. R, 2014, arXiv, arXiv:1401.1389
Li Y., et al., 2007, ApJ, 665, 187
Lukić, Z., Heitmann, K., Habib, S., Bashinsky, S., & Ricker, P. M. 2007, ApJ, 671, 1160
Lukić, Z., Reed, D., Habib, S., & Heitmann, K. 2009, ApJ, 692, 217
Lupton R., Blanton M. R., Fekete G., Hogg D. W., O'Mullane W., Szalay A., Wherry N., 2004, PASP, 116, 133
Madau P., Ferguson H. C., Dickinson M. E., Giavalisco M., Steidel C. C., Fruchter A., 1996, MNRAS, 283, 1388
Marulli F., et al., 2013, A&A, 557, A17
McGreer I. D., et al., 2013, ApJ, 768, 105
Merloni, A., Bongiorno, A., Bolzonella, M., et al. 2010, ApJ, 708, 137
Monaghan J. J., 1992, ARA&A, 30, 543
More, S., Kravtsov, A. V., Dalal, N., & Gottlöber, S. 2011, ApJS, 195, 4
Moreland, K., 2009, Proceedings of the 5th International Symposium on Advances in Visual Computing: Part II, Pages 92-103, Springer-Verlag, Berlin, Heidelberg
Oppenheimer, B. D., & Davé, R. 2006, MNRAS, 373, 1265
Orban C., 2013, arXiv, arXiv:1312.5256
Pelupessy F. I., Di Matteo T., Ciardi B., 2007, ApJ, 665, 107
Pérez-González P. G., et al., 2008, ApJ, 675, 234
Planck Collaboration, et al., 2013, arXiv, arXiv:1303.5076
Press, W. H., & Schechter, P. 1974, ApJ, 187, 425
Reed, D. S., Bower, R., Frenk, C. S., Jenkins, A., & Theuns, T. 2007, MNRAS, 374, 2
Ross N. P., et al., 2013, ApJ, 773, 14
Sawala, T., Frenk, C. S., Crain, R. A., et al. 2013, MNRAS, 431, 1366
Sato M., Matsubara T., 2013, PhRvD, 87, 123523
Scannapieco C., et al., 2012, MNRAS, 423, 1726
Scherrer R. J., Weinberg D. H., 1998, ApJ, 504, 607
Shakura N. I., Sunyaev R. A., 1973, A&A, 24, 337
Shen Y., et al., 2009, ApJ, 697, 1656
Sheth, R. K., & Tormen, G. 1999, MNRAS, 308, 119

Sheth, R. K., & Tormen, G. 2002, MNRAS, 329, 61
Sijacki D., Springel V., Di Matteo T., Hernquist L., 2007, MNRAS, 380, 877
Sijacki D., Springel V., Haehnelt M. G., 2009, MNRAS, 400, 100
Sirko, E. 2005, ApJ, 634, 728
Springel, V., White, S. D. M., Tormen, G., & Kauffmann, G. 2001, MNRAS, 328, 726
Springel V., Hernquist L., 2003, MNRAS, 339, 289
Springel V., Hernquist L., 2003, MNRAS, 339, 312
Springel V., Di Matteo T., Hernquist L., 2005, MNRAS, 361, 776
Springel V., 2005, MNRAS, 364, 1105
Springel V., et al., 2005, Natur, 435, 629
Springel V., 2010, MNRAS, 401, 791
Springel V., 2012, AN, 333, 515
Tinker, J., Kravtsov, A. V., Klypin, A., et al. 2008, ApJ, 688, 709
Tomczak A. R., et al., 2013, arXiv, arXiv:1309.5972
Torrey, P., Vogelsberger, M., Genel, S., et al. 2014, MNRAS, 38
Vogelsberger, M., Genel, S., Sijacki, D., et al. 2013, MNRAS, 436, 3031
Volonteri M., Rees M. J., 2006, ApJ, 650, 669
Wang R., et al., 2010, ApJ, 714, 699
Wang R., et al., 2011, AJ, 142, 101
Warren, M. S., Abazajian, K., Holz, D. E., & Teodoro, L. 2006, ApJ, 646, 881
Watson, W. A., Iliev, I. T., D'Aloisio, A., et al. 2013, MNRAS, 433, 1230
Wilkins S. M., Bunker A., Coulton W., Croft R., Matteo T. D., Khandai N., Feng Y., 2013, MNRAS, 430, 2885
Wilkins S. M., Di Matteo T., Croft R., Khandai N., Feng Y., Bunker A., Coulton W., 2013, MNRAS, 429, 2098
Wilkins S. M., et al., 2013, MNRAS, 435, 2885
White, M., Hernquist, L., & Springel, V. 2001, ApJL, 550, L129
White, M. 2002, ApJS, 143, 241
Zheng, Z., Berlind, A. A., Weinberg, D. H., et al. 2005, ApJ, 633, 791